Weakening of cold halocline layer exposes sea ice to oceanic heat in the eastern Arctic Ocean

Polyakov, Igor ; Rippeth, Tom; Fer, Ilker; Alkire, Matthew; Baumann, Till; Carmack, Eddy; Ivanov, Vladimir; Janout, M.A.; Padman, Laurie; Pnyushkov, Andrey; Rember, Robert

Journal of Climate

DOI:
10.1175/JCLI-D-19-0976.1

Published: 15/09/2020

Publisher's PDF, also known as Version of record

Weakening of cold halocline layer exposes sea ice to oceanic heat in the eastern Arctic Ocean

Igor V. Polyakov[1*], Tom P. Rippeth[2], Ilker Fer[3], Matthew B. Alkire[4], Till M. Baumann[1], Eddy C. Carmack[5], Randi Ingvaldsen[6], Vladimir V. Ivanov[7], Markus Janout[8], Sigrid Lind[6], Laurie Padman[9], Andrey V. Pnyushkov[10], Robert Rember[10]

1 *International Arctic Research Center and College of Natural Science and Mathematics, University of Alaska Fairbanks, 930 Koyukuk Drive, Fairbanks, AK, 99775, USA and Finnish Meteorological Institute, Erik Palménin aukio 1, 00560 Helsinki.*

2 *School of Ocean Sciences, Bangor University, Menai Bridge, LL59 5AB, United Kingdom.*

3 *Geophysical Institute, University of Bergen and Bjerknes Centre for Climate Research, Bergen, Norway.*

4 *Polar Science Center, Applied Physics Lab, University of Washington, 1013 NE 40th Street, Seattle, WA 98105, USA.*

5 *Institute of Ocean Sciences, Fisheries and Oceans Canada, 9860 West Saanich Road, Sidney, BC, V8L 4B2, Canada.*

6 *Institute of Marine Research, Strandgaten 196, N5817 Nordnes, Bergen, Norway.*

7 *International Arctic Research Center, University of Alaska Fairbanks, 930 Koyukuk Drive, Fairbanks, AK, 99775, USA, Lomonosov Moscow State University, Geography Department, 1, Leninskiye Gory, Moscow 119991 Russia.*

8 *Alfred Wegener Institute, Helmholtz Centre for Polar and Marine Research, Am Handelshafen 12, D-27570 Bremerhaven, Germany.*

9 *Earth and Space Research, Corvallis, OR, USA.*

10 *International Arctic Research Center, University of Alaska Fairbanks, 930 Koyukuk Drive, Fairbanks, AK, 99775, USA.*

[*]Corresponding author: Igor Polyakov, 907-474-2686, ivpolyakov@alaska.edu

Early Online Release: This preliminary version has been accepted for publication in *Journal of Climate*, may be fully cited, and has been assigned DOI 10.1175/JCLI-D-19-0976.1. The final typeset copyedited article will replace the EOR at the above DOI when it is published.

Abstract:

A 15-year duration record of mooring observations from the eastern (>70^{o}E) Eurasian Basin (EB) of the Arctic Ocean is used to show and quantify the recently increased oceanic heat flux from intermediate-depth (~150-900 m) warm Atlantic Water (AW) to the surface mixed layer (SML) and sea ice. The upward release of AW heat is regulated by the stability of the overlying halocline, which we show has weakened substantially in recent years. Shoaling of the AW has also contributed, with observations in winter 2017-2018 showing AW at only 80 m depth, just below the wintertime surface mixed layer (SML), the shallowest in our mooring records. The weakening of the halocline for several months at this time implies that AW heat was linked to winter convection associated with brine rejection during sea ice formation. This resulted in a substantial increase of upward oceanic heat flux during the winter season, from an average of 3-4 W/m^2 in 2007-2008 to >10 W/m^2 in 2016-2018. This seasonal AW heat loss in the eastern EB is equivalent to a more than a two-fold reduction of winter ice growth. These changes imply a positive feedback as reduced sea ice cover permits increased mixing, augmenting the summer-dominated ice-albedo feedback.

Keywords: Arctic Ocean, climate change, stratification, sea ice, ocean mixing

Accepted for publication in *Journal of Climate*. DOI 10.1175/JCLI-D-19-0976.1.

1. Introduction

In recent decades there has been a dramatic decline in seasonal sea ice extent in the Arctic Ocean, with a more recent year-around decline in sea ice extent, area and volume (Kwok 2018; Stroeve and Notz 2018). This change has shifted the local radiative balance resulting in a positive ice-albedo feedback mechanism as increasing lead fraction and surface melt pond areas in decaying Arctic sea ice facilitate enhanced upper-ocean solar heating and more rapid melting of ice floes (e.g., Perovich et al. 2008; Toole et al. 2010). Moreover, it was hypothesized that the declining sea ice has larger scale hemispheric impacts on the North Atlantic Oscillation and, in consequence, mid-latitude weather patterns (e.g., Francis et al. 2017; Garcia-Serrano et al. 2015; Kolstad and Screen 2019).

Heat associated with oceanic currents originating from lower latitudes provides an important, and year-round, source of heat to the Arctic Ocean (e.g., Carmack et al. 2015). The dominant external source of oceanic heat is the warm (temperature >0^{o}C) and salty water of Atlantic origin (Atlantic Water, AW) which is distributed throughout the deep basins at intermediate depths (~150-900 m, **Fig. 1**) and holds sufficient heat to melt the Arctic sea ice 3-4 times over (Carmack et al. 2015). Across much of the eastern (>70^{o}E) Eurasian Basin (EB) this heat is isolated from the surface, and hence the sea ice, by large vertical density gradients associated with the Arctic halocline (60-150 m, **Fig. 1**). The presence of the halocline impedes the transport of AW heat upward towards the surface across much of the Arctic Ocean (e.g., Fer 2009). The exception to this is the western (<70^{o}E) Nansen Basin where substantial turbulent mixing linked to the tides (Fer et al. 2010; Padman and Dillion 1991; Rippeth et al. 2015; Renner et al. 2019) and wind events (e.g. Provost et al., 2017; Graham et al., 2019) supports heat fluxes in excess of 50 W m^{-2}

Accepted for publication in *Journal of Climate*. DOI 10.1175/JCLI-D-19-0976.1.

Inflowing AW is warming (Barton et al. 2018) driving a regime shift in sea ice cover over the past decade in the Barents Sea (Onarheim et al. 2018). There is also a growing body of evidence that the characteristics of the Arctic halocline are changing; for example, the halocline has weakened in the eastern EB since the 1970s (Steele and Boyd 1998; Polyakov et al. 2010). These changes have accelerated over the past decade (Polyakov et al. 2020a) with continuous time series from moored instruments capturing the significant weakening of the cold halocline layer (the upper part of the halocline with temperatures near freezing and negligible vertical temperature gradient) and shoaling of the AW in 2013-2015 (Polyakov et al. 2017).

The combination of weaker stratification and shoaling of the AW in the EB, coupled with the loss of sea ice, has allowed progressively deeper winter ventilation in the eastern EB in recent years (Polyakov et al. 2017). This process further enhances the annually averaged upward AW heat fluxes. The shift in sea ice state and upper ocean stratification to conditions previously unique to the western Nansen Basin has been termed 'atlantification' (Polyakov et al. 2017) and represents a transition toward a new Arctic climate state, in which the geographical influence of the AW heat on sea ice volume is spreading eastwards.

Since the increased oceanic heat fluxes associated with atlantification drive sea ice melt, and reduced sea ice increases oceanic heat fluxes through increased convective entrainment in winter, this process represents a positive ice/ocean-heat feedback mechanism. This mechanism is analogous and complementary to the ice-albedo feedback, in which atmospheric warming leads to a reduction of ice and snow coverage and decreasing albedo, resulting in further snow and sea ice retreat (Manabe and Stouffer 1980).

The strength of the ice/ocean-heat feedback is determined by the vertical flux of AW heat across the halocline into the surface-forced seasonal convective layer. Polyakov et al. (2017)

Accepted for publication in *Journal of Climate*. DOI 10.1175/JCLI-D-19-0976.1.

estimated seasonal changes of heat content Q in the eastern EB halocline (65-130 m) and an equivalent divergent heat flux (the difference of fluxes at two depth levels for which a 1D equation of heat balance for a unit-area water column is integrated) of δF_h ~12 W m^{-2} over this depth range for winter 2013-2014, and ~8 W m^{-2} for winter 2014-2015. They argued that these inferred values of δF_h exceeded previous regional estimates (e.g., Lenn et al. 2009; Polyakov et al. 2013) by a factor of 2-4 and potentially account for an additional loss of up to 18-40 cm of sea ice over this period of time associated with the increase in upward AW heat transport. In consequence the impact of the oceanic heat flux on sea ice formation in 2013-2015 was comparable to that of the atmospheric thermodynamic forcing (Polyakov et al. 2017).

The aim of this paper is to quantify the changes in the upper ocean heat content, and the consequent release of heat from the AW up into the halocline and to the surface mixed layer in the key eastern Eurasian Basin of the Arctic Ocean. We improve on the Polyakov et al. (2017) study by including new data collected over the period 2015-2018 to quantify changes in the upper ocean heat content, and the consequent release of heat from the AW up into the halocline and to the surface mixed layer in the EB. We then compare these regional estimates with earlier estimates.

2. Data

Our analyses utilize observations of ocean temperature, salinity, and currents from moorings deployed in the eastern EB (**Fig. 2, Table 1**). Observations at the M1$_4$ mooring site began in August 2002, with several co-located moorings deployed and recovered annually prior to 2009, and longer duration of deployments since 2013 (**Table 1**).

Moorings deployed in summer 2013 and recovered in summer 2015 provided two-year long records for most instruments except for the M1$_5$ upper ocean Acoustic Doppler Current Profiler (ADCP), which worked for 10 months only. Mooring M3 located off Severnaya Zemlya, was

Accepted for publication in *Journal of Climate*. DOI 10.1175/JCLI-D-19-0976.1.

deployed at water depth of 1350 m. Six moorings ($M1_1$-$M1_6$) formed a ~350-km cross-slope section spanning from the 250 m to 3400 m isobaths along 126°E. Topographically steered boundary current flows along slope across this section (Pnyushkov et al. 2015, 2018). Averaged over 2013-2015, the maximum current speed of ~11 cm/s was found at the shallowest mooring $M1_1$ (on the 250 m isobath), with only ~0.5 cm/s in the deep basin at moorings $M1_5$ and $M1_6$. The AW core defined by the maximum water temperature is typically located at the $M1_5$ mooring site at a depth of ~250 m.

Deployment of moorings in 2015-2018 repeated the mooring distribution used for 2013-2015 except that the $M1_6$ mooring was not re-deployed (**Table 1**). Almost all mooring instruments provided full three-year long records; the $M1_3$ McLane Moored Profiler (MMP) stopped recording after two years. In addition, a short-term mooring, $M1_{4\text{-short}}$, was deployed for 18 days only (September 2–20, 2018) close to the $M1_4$ climatologic mooring site (**Table 1**). The short-term mooring was designed to provide current and CTD data with the most rapid possible sampling rate in the upper 200 m.

Mooring Conductivity-Temperature-Depth (CTD) data: The MMP-based moorings at the $M1_4$ mooring location in 2002-2009 collected temperature, salinity and current velocity profiles once per day. Four 2013-2015 moorings ($M1_2$, $M1_3$, $M1_5$, and $M1_6$) and two 2015-2018 moorings ($M1_3$ and $M1_5$) provided vertical MMP profiles with two-day sampling interval with a ~0.25 m spacing. The MMPs on most moorings sampled the 50–700 m depth range; however, the 2015-2018 $M1_5$ mooring missed its target depth and the MMP record only reached to ~170 m below the surface. The MMP on the $M1_{4\text{-short}}$ mooring sampled about every 18 minutes and obtained 1369 profiles. The MMP temperature and conductivity calibrated measurement accuracies are ±0.002˚C and ±0.002 mS/cm.

Accepted for publication in *Journal of Climate*. DOI 10.1175/JCLI-D-19-0976.1.

154 The moorings $M1_1$, $M1_2$, $M1_4$ and M3 with no MMP profilers deployed in 2013–2018, as
155 well as mooring M1g, deployed about 12 km from mooring $M1_4$ in 2008 –2010 (**Fig. 2, Table 1**)
156 were equipped with Seabird SBE-37 CTD instruments and provided records of conductivity,
157 temperature and pressure with sampling interval of one hour or shorter, with measurement
158 accuracies for temperature and conductivity of ±0.002˚C and ±0.003 mS/cm, respectively.

159 *Mooring current data*: Most moorings used in this analysis included 300 kHz Acoustic
160 Doppler Current Profilers (ADCP) targeting the upper 50-60 m of the water column (**Table 1**).
161 Moorings with no MMP were also equipped by long-range ADCP 75 kHz covering deeper layers
162 (**Table 1**). ADCPs provided current velocities, averaged over 2-m (prior to 2013) or 4-m (after
163 2013) vertical cells, with 1-h time resolution. The manufacturer's estimates for ADCP accuracies
164 are 0.5% of measured speed and 2° for current direction.

165 Moorings equipped with MMPs provided current velocity profiles with above mentioned
166 profiling intervals and 0.25 m vertical resolution. The MMPs were equipped with a Falmouth
167 Scientific Inc. (FSI) micro-CTD sensor in 2002-2004 and a Sea-Bird Electronics (SBE) 41CP
168 CTD sensor starting from 2004, with temperature and conductivity measurement accuracies of
169 about ±0.002˚C and ±0.0003 S/m, respectively. Prior to 2013, the MMPs carried the FSI
170 Acoustic Current Meters (ACM); after 2013, the ACMs were substituted with the FSI ACM-
171 PLUS-MP (http://www.falmouth.com/product-information.html). The velocity precision of the
172 FSI ACM (ACM-PLUS-MP) carried on the MMP are reported to be ±2% (1%) of reading and
173 ±0.5 cm/s for velocity resolution. Compass accuracy is ±2˚. All MMP sensors were calibrated
174 before their deployment and immediately after their recovery using McLane facilities.

175 *Ship-borne CTD data*: Mooring observations were complemented by repeated hydrographic
176 profiles collected using a Seabird SBE911plus CTD system in 2013, 2015 and 2018 at $M1_4$

Accepted for publication in *Journal of Climate*. DOI 10.1175/JCLI-D-19-0976.1.

mooring site (**Fig. 2**). The effective vertical resolution, considering the different sensor characteristics, is about 25 cm. Individual temperature and conductivity measurements are accurate to ±0.002˚C and ±0.0003 S/m.

3. Methods

Defining a proxy for Richardson (Ri) number: *Ri* is a measure of the stability of the water column, *ie*. when $Ri < 0.25$ the vertical shear in the flow is sufficient to generate instability and turbulent mixing. As such *Ri* estimates provide a useful indicator for the likelihood of shear instability/ mixing. The correct scale for the estimation of *Ri* is the Ozmidov scale (which in this case we estimate to be $O(0.1\text{m})$). However, the vertical resolution of the *Ri* estimate is limited by the positions of instruments on the moorings which have a vertical resolution of 20m. Whilst the 20 m *Ri* estimates are likely to smooth out the fine structure of individual instabilities, we argue that the smaller the large-scale *Ri* value is, the greater the likelihood of shear instability (and so turbulence and mixing). As such the 20m *Ri* provides a useful proxy for the likelihood of shear instability. Moreover, trends in the 20m (proxy) *Ri* estimate will expose trends in the likelihood of shear instability, the key interpretation here. This approach is supported by direct comparisons of dissipation and low resolution *Ri* estimates (e.g. Mead Silvester et al., 2014).

The mooring-based estimates of *Ri* (**Fig. 5**) are based on MMP measurements of stratification and velocity. Stratification over the 100-140 m layer is quantified using buoyancy frequency (N), $N^2 = -(g/\rho_o)\partial\rho/\partial z$, where ρ is the potential density of seawater, ρ_o is the reference density (1030 kg m^{-3}), and g is the acceleration due to gravity. The limited depth range of 100-140m was chosen due to insufficient data coverage in early years (see **Table 1**). The *Ri* proxy was estimated as $Ri = N^2/|\mathbf{U}_z|^2$, where $|\mathbf{U}_z|$ is the magnitude of the vertical shear of the horizontal

Accepted for publication in *Journal of Climate*. DOI 10.1175/JCLI-D-19-0976.1.

199 currents; $|\mathbf{U}_z|$ and N were calculated averaging gradients over 20 m vertical scale for all points
200 within the 100-140 m depth range.

201 *Defining timing and depth of seasonal upper ocean ventilation and divergent heat flux δF_h :*
202 For this analysis, temperature observations carried out by $M1_2$, $M1_3$, $M1_4$ and M3 moorings in
203 2013–2018 were used. SBE-37 data from non-MMP moorings $M1_2$ (2015–2018), $M1_3$, $M1_4$ and
204 M3 were complemented by MMP profiles from $M1_2$ (2013 –2015) mooring. SBE-37
205 observations were linearly interpolated to match the MMP vertical resolution. We are interested
206 in the analysis of seasonal ventilation of the halocline. Accordingly, temperature observations
207 were filtered using wavelet transformations to keep seasonal variations only (and thus different
208 temporal sampling by MMP and SBE-37 did not affect our results). A standard package of
209 wavelet programs was used based on the DOG Mother function. Estimates of heat content (Q,
210 J/m^3, with freezing point taken as a reference temperature at a given salinity) for the halocline
211 (65-140 m) are shown in **Fig. 6**. To assure that the use of SBE-37 point measurements with
212 relatively coarse vertical resolution and continuous MMP profiles for estimates of Q did not
213 affect our results we calculated Q using MMP temperature record from $M1_2$ mooring (2015–
214 2018) twice, first time with original MMP resolution and another one with sub-sampled coarser
215 resolution matching SBE-37 depth levels (**Table 1**). Results of Q integrated over the halocline
216 depth range and averaged in time over the entire record length differed by 8%.

217 The aim is to define the timing and amplitude of upward heat flux associated with winter
218 ventilation. To this end, we identified timing and amplitude of the maximum Q (as accumulated
219 over the warm phase of the seasonal cycle) and the minimum of Q (associated with winter
220 ventilation) using Q vertically integrated over 65-140 m. The depth of the ventilation is defined

Accepted for publication in *Journal of Climate*. DOI 10.1175/JCLI-D-19-0976.1.

as the deepest point where a distinct minimum of Q was found. The maximum of vertically integrated Q was then re-calculated using the depth of ventilation.

Following Polyakov et al. (2017), we limited the boundary of the winter ventilation layer to 140 m. For some years, the boundary of the layer was deeper (as shown in **Fig. 6** by the black horizontal segments located at the very bottom of the panels with Q). Therefore, our choice of the ventilation layer is conservative and estimates of divergent heat fluxes δF_h derived from change of heat content ΔQ during each winter season represent the lower bound, consistent with the objectives of the study. For the upper boundary of the layer for which Q is estimated, we selected the depth 65 m, chosen because this best determines the halocline layer in which heat from the AW is stored and released (Polyakov et al. 2013, 2017). We evaluated the sensitivity of our estimates to the choice of the boundary of the ventilation layer by calculating δF_h for 65-140 m and 65-150 m layers. The 10 m increase in layer thickness increases δF_h by less than 8%.

Following Polyakov et al. (2013), we estimated δF_h (W/m^2) between two depth levels as the change, in time, of vertically integrated Q. This approach is based on the assumption that all change in heat content is due to vertical exchange (so 1D). Note that these values are flux *differences* between two depth levels, and total heat fluxes may be larger than these values due to additional non-divergent heat transports; thus, our inferred estimates of divergent heat fluxes represent *lower* bounds for the total heat flux (for details, see Polyakov et al. 2013).

4. Results

a. AW warming and weakening of halocline stratification in the eastern Eurasian Basin

Time series of the AW temperature show significant interannual variability (**Fig. 3a**). The AW in the eastern EB began warming in the early 2010s, with the AW temperature in 2018 being, on

Accepted for publication in *Journal of Climate*. DOI 10.1175/JCLI-D-19-0976.1.

243 average, 0.5–0.7°C higher than in 2011 (**Fig. 3a**). This recent warming is particularly noticeable
244 at shallower depths, with the increase in temperature at 150 m exceeding 1.5°C between 2011
245 and 2018. This warming over the depth range 150-750 m between September 2013 – May 2014
246 and September 2016 – May 2017 is partially associated with shoaling of the upper halocline
247 boundary (**Fig. 3c**) and a substantial increase in AW layer thickness (**Fig. 4**).

248 Cross-correlation analysis of time series of AW temperature measured at 250m from 1997-
249 2018 in Fram Strait, the entry point of AW into the Arctic, and from 2002-2018 in the eastern EB
250 (red time series in **Fig. 3a**) shows the strongest correlation, $R = 0.67$, for a lag of 682 days (Fram
251 Strait series leads, **Fig. 3b**). The fit between the two time series is better over the last 7-8 years
252 than it is over the earlier period. The ~2 year lag suggests that warm pulses of AW that entered
253 the Arctic Ocean through Fram Strait, are traveling towards the eastern EB at a speed 2-2.5 time
254 faster than that estimated for a warm AW pulse which entered the eastern EB in 2004 (Polyakov
255 et al. 2005). This implies that the rate of advection has increased over time. However, noisy data
256 due to gaps in the EB record preclude meaningful statistical analysis using just the early part of
257 the time series. Assuming that the lagged correlation between the two time series will persist in
258 the near future, the latest part of the Fram Strait series (not shown) implies that the AW
259 temperature in the eastern EB reached its peak in late 2018 (these data are not yet available) and
260 will slowly decrease over the next 1-2 years.

261 Temperature and salinity profiles in the eastern EB from CTD during 2013-2018 and MMP
262 during 2003-2018 recorded a decline of stratification (N^2) over the 110-140m depth range of the
263 halocline (**Figs. 1c, 5a,b**) which may be a result of both the shoaling of AW and weakening of
264 halocline stratification. Polyakov et al. (2018) used available potential energy defined for the
265 variable-depth halocline to show overall weakening stratification in the EB since the 1980s, with

Accepted for publication in *Journal of Climate*. DOI 10.1175/JCLI-D-19-0976.1.

accelerated tendencies in the 2010s compared with the 2000s. However, the substantial weakening of halocline stability from 2013 to 2015 (Polyakov et al. 2017) which continued in 2015–2018, and which was also partially associated with shoaling of the AW (**Fig. 4**) found at 80 m depth, as inferred from the most recent observations in winter 2017-2018 (**Figs. 3c**). This represents the shallowest depth the AW has been observed in the 15 years of mooring deployments. As these estimates used a linear interpolation of CTD time series made at 38m and 107m at mooring $M1_4$, we are not able to definitively conclude that the cold halocline layer was present (albeit very thin) during the winter of 2017–2018. However, the record suggests the extreme thinning (or even absence) of the Arctic cold halocline layer for several months at this time (**Figs. 3c, 4**) implying that AW heat was exposed to winter convection associated with sea ice formation and brine rejection.

b. Increased oceanic heat fluxes and ice loss in the eastern Eurasian Basin

The weakening stratification, shoaling of the AW layer and increase of current shear in recent years (e.g., Polyakov et al. 2020b) have altered the seasonal cycle of upward AW heat transport (**Fig. 6**). Estimated change in heat content (Q) from the halocline (65-140 m) during winter, averaged at four moorings, is equivalent to mean divergent heat fluxes (Section 3) of δF_h = 12.0±5.5, 3.5±2.2, 3.0±1.9, 12.9±1.7 and 20.6±6.8 W/m^2 for five winters from 2013-2014 through 2017-2018 (**Figs. 6, 7**). For three of these winters (2013-2014, 2016-2017, and 2017-2018), δF_h greatly exceeded (3- to 5-fold) the previous estimates derived from summer 2007-2008 microstructure observations over the Laptev Sea slope (Lenn et al. 2009; Polyakov et al. 2019) and winter 2009-2010 ITP-37 observations in the central Amundsen Basin (Polyakov et al. 2013). For the winters of 2014-2015 and 2015-2016, estimates of δF_h were comparable to upward heat fluxes of about 3-4 W m^{-2} from 2007-2008. We attribute the decrease of δF_h in

Accepted for publication in *Journal of Climate*. DOI 10.1175/JCLI-D-19-0976.1.

289 2015-2016 (cf. Polyakov et al. 2017) to an anomalous freshening event in the upper ocean. This
290 freshening is evident in data collected at mooring $M1_3$ (**Fig. 8)** which shows that strong upper
291 (<75 m) ocean stratification (evidenced by high N^2 values) in 2016 precluded seasonal
292 ventilation beyond the SML. Stronger stratification in winter 2015 (compared with winters of
293 2014 and 2017, **Fig. 8d**) limited seasonal ventilation to the upper ~115m, thus not extending
294 deeply enough to reach the main pool of AW heat (**Fig. 8b**). In consequence the heat flux is
295 limited. The strongest heat flux is inferred for winter 2017-2018 and is associated with the
296 weakest stratification (**Fig. 5**), providing further evidence for the key role of stratification in
297 mediating upper ocean ventilation.

298 The new estimates of seasonal ventilation of heat evaluated from the δF_h for the winter
299 seasons of 2016-2017 and 2017-2018 are equivalent to 78±4 and 93±29 cm reductions in ice
300 growth, respectively, for the eastern EB (**Fig. 7)**, given that one year of a heat flux of 1 W/m^2 in
301 isolation is equivalent to about 10 cm of sea ice loss. This represents a two-fold increase in the
302 sea ice loss rate compared to that estimated for 2013-14 (54 cm) and 2014-2015 (40 cm)
303 (Polyakov et al. 2017), and so partially explains intensified eastern EB sea ice loss in more recent
304 years (Onarheim et al. 2018; Stroeve and Notz 2018).

305 Time series from the shallower moorings ($M1_2$ and $M1_3$) show strong seasonal variations in
306 the AW core temperature, which may be associated with seasonal displacement of the AW core
307 relative to the slope (e.g., Baumann et al. 2018). However, the consistently low correlation
308 between *Q* and the AW core temperature records, for all mooring sites (**Fig. 9**), implies that
309 cross-slope shifts in AW temperature core are not a major driver of the seasonal variation in *Q* in
310 the halocline. The correlation between *Q* and AW core temperature at the shallowest mooring
311 ($M1_2$) where currents are strongest is also weak (R = 0.29) indicating that advection does not

Accepted for publication in *Journal of Climate*. DOI 10.1175/JCLI-D-19-0976.1.

312 provide a significant contribution to the seasonal variability of *Q*. This evidence is consistent
313 with the results of Polyakov et al. (2017) who argued that the in-phase seasonal maxima and
314 minima of wavelet transforms of *Q* at all mooring sites suggests that the observed winter
315 ventilation is driven by surface cooling and sea-ice formation—and not by lateral advection.
316 They reasoned that spatially varying water transports across the slope, ranging from 13 cm/s
317 (measured over the upper continental slope (250-700 m) by moorings $M1_1$ and $M1_2$) to 1-2 cm/s
318 (measured at 2700 m and deeper, at mooring locations $M1_4$, $M1_5$ and $M1_6$) make the in-phase
319 pattern of the seasonal signal at all moorings impossible to explain using the advective
320 mechanism. Furthermore, mooring $M1_6$ which was farthest from the near-slope boundary
321 current, in the ocean interior, yielded estimates for F_h which magnitudes and phases are
322 consistent with estimates from the other moorings deployed on the eastern EB continental slope
323 in 2013–2015 (Polyakov et al., 2017).

324 The one-dimensional approach adopted here can be further validated by considering the
325 magnitude of the lateral temperature gradient necessary to explain the estimated heat flux, if
326 advection were to dominate. In assuming an along slope current speed of 2 cm/s requires that the
327 lateral temperature gradient dT/dx must be five times larger than that observed Fram Strait –
328 central Laptev Sea slope temperature decrease of 1.8ºC [= 3.0 – 1.2] over ~2400km so dT/dx =
329 0.75×10^{-3} ºC/km to explain the estimated heat flux. Another potential contributor to the observed
330 ventilation rates are lateral eddy fluxes. Ventilation of halocline by eddies is, however, difficult
331 to quantify using available data. Nevertheless, considering that the typical time of eddy passing
332 across the mooring site is about a week with the average frequency about one eddy per
333 month (Pnyushkov et al., 2018b), it is unlikely that eddies can significantly contribute to changes

Accepted for publication in *Journal of Climate*. DOI 10.1175/JCLI-D-19-0976.1.

of the heat content at seasonal time scales. These considerations imply the uncertainty in the 1D flux calculation from lateral advection and diffusion is small.

5. Discussion and Conclusions

Time series measurements from a 15-year mooring record in the eastern EB of the Arctic Ocean demonstrate that the previously identified weakening of stratification over the halocline, which isolates intermediate depth AW from the sea surface, over the period 2003 - 2015 (e.g., Polyakov et al. 2017, 2018), has continued at an increasing rate in more recent years (2015-2018). In consequence, oceanic heat fluxes for the winters of 2016-2018 are estimated to be greater than 10 Wm^{-2}. These fluxes are substantially larger than the previously reported winter estimates for the region for 2007-2008 of 3-4 Wm^{-2} (Lenn et al., 2009; Polyakov et al., 2019), and comparable to the estimates for the winters of 2013-2015 (Polyakov et al. 2017), implying a significant enhancement of the role of oceanic heat in this region in recent years.

Moreover, the increased vertical heat fluxes have been accompanied by increased upper-ocean current speeds $|\mathbf{U}|$ and the vertical shear in the horizontal velocities $|\mathbf{U}_z|$ over the period 2015–2018 (Polyakov et al. 2020b). Using mooring observations from 2003 to 2018, these authors showed that $|\mathbf{U}|$ and $|\mathbf{U}_z|$ in the upper 60 m of the water column increased by about 20% and 40%, respectively. In the lower halocline (110-140 m), $|\mathbf{U}|$ was generally larger after 2008, increasing on average from 2.5-3.5 cm/s in 2003–2008 to about 4-5 cm/s in 2009–2018 (**Fig. 5c,d**) although the change was not as strong in very recent years, 2016 and 2018 when compared to 2009–2015. There is also clear transition in |Uz|, with significantly larger shears evident post-2010, and in particular in the summer of 2018 (**Fig. 5c,d**). However, Pnyushkov et al. (2018) found no significant change in the mean along-slope water transport over the same period.

Accepted for publication in *Journal of Climate*. DOI 10.1175/JCLI-D-19-0976.1.

356 The combination of reduced stratification and increased shear implies a decreases the gradient
357 Richardson number, *Ri*, defined in section 3 (**Fig. 5e,f**), consistent with an increased turbulent
358 heat flux, associated with vertical mixing by shear instabilities. Although the *Ri* estimates are
359 based on 20m vertical resolution measurements, they show a clear trend towards reduced
360 dynamic stability which may be interpreted as a tendency towards increased turbulent mixing in
361 recent years, coincident with the increase in maximum halocline heat content (**Fig. 6**). This
362 tendency is particularly strong in 2018 with amplified velocity shear in the relatively weakly
363 stratified upper ocean (**Fig. 5**).
364 The increased shear and weakening of stratification as prerequisites for enhanced turbulent
365 mixing are consistent with the recent transition in the upper ocean to conditions previously
366 unique to the western Nansen Basin, a process called 'atlantification' (Polyakov et al. 2017).
367 Our analyses confirm that, in part, the loss of stratification in the eastern EB halocline can be
368 attributed to processes originating upstream. For example, the change in halocline salinity, the
369 main contributor to water column stability in the eastern EB, is correlated with upper ocean
370 salinity changes in the northern Barents Sea with a lag of approximately 2 years (**Fig. 10**) (Lind
371 et al. 2018), revealing coherent interannual variability between the two regions. In the Barents
372 Sea, these changes were found to be closely linked to declines in sea ice imports to the Barents
373 Sea (Lind et al., 2018; Barton et al., 2018). The shift towards higher salinities in the eastern EB
374 lag the changes in the northern Barents Sea by about 1 year (**Fig. 10**), implying an eastward
375 lateral progression of the 'atlantification'. Shelf-basin interactions may also be contributing to
376 the observed warming (e.g. Timmermans et al., 2018).
377 Our observations point to the shift of this region of the eastern Arctic Ocean towards a new
378 regime that is more typical of the continental slope regions of the western Nansen Basin where

Accepted for publication in *Journal of Climate*. DOI 10.1175/JCLI-D-19-0976.1.

surface conditions are strongly influenced by oceanic heat imported from the Atlantic Ocean (**Fig. 11**). The flux of AW heat to the sea ice cover and the atmosphere has increased, during the winter season, from an average of 3-4 W/m^2 in 2007-2008 to >10 W/m^2 in 2016-2018, equivalent to more than a two-fold reduction of winter ice growth over the last decade.

The process described here represents a positive feedback, analogous to the ice-albedo feedback, since increased ocean heat flux to the sea surface reduces ice thickness and increases its mobility, increasing atmospheric momentum flux into the ocean and reducing the damping of surface-intensified baroclinic tides (Carr et al., 2019). We refer to this process as the "ice/ocean-heat" feedback. As with the ice-albedo feedback, the contribution of the ice/ocean-heat feedback to long-term sea ice trends depends on the seasonal variability of several factors that affect mixing rates including sea ice concentration and thickness, baroclinic tidal response to seasonally varying stratification, and wind stress impacts on sea ice and on AW shoaling. The transition in dominant mixing regime from double diffusion to shear-driven mixing also affects the relative magnitudes of buoyancy fluxes due to heat and salinity transports; the vertical diffusivities for heat and salt are the same in shear-driven turbulence, but are different for double diffusion (Kelley, 1984). Coincident vertical nutrient fluxes, which support oceanic primary productivity, food web structure and carbon export from the atmosphere to the seabed (Bluhm et al. 2015; Falk-Peterson et al. 2015), will also increase. Moreover, the nutricline has shoaled in recent years (relieving nutrient limitations, **Fig. 1d**) which coupled with declining sea ice cover (relieving light limitations), both influenced by atlantificiation, and so could lead to regional-scale enhancement of biological productivity in the central Arctic Ocean.

As ice thins – through atmospheric forcing, changing ocean heat fluxes, and feedbacks – upper-ocean stratification is responding and a new Arctic state is emerging which may not be

Accepted for publication in *Journal of Climate*. DOI 10.1175/JCLI-D-19-0976.1.

easily reversed. For example, a large anomaly in AW heat input coupled with shoaling may lead, through the ice/ocean-heat feedback, to an expanding and more permanent Atlantic-dominated state wherein the hydrographic structure of the halocline no longer provides sufficient insulation between the intermediate depth AW and the sea ice, even when the heat flux associated with the AW is relaxed. This potential for a permanent transition of the eastern Arctic to a new state, emphases the pressing need for the incorporation of improved mixing schemes into Arctic climate models in order that they better simulate the evolving halocline stratification and its impact on sea ice state.

Appendix A1. Building Long-Term Time Series

Changes in the 110-140 m (halocline) layer at the $M1_4$ mooring site shown in **Fig. 5** were documented using MMP records for 2003-2007 and 2013-2018, SBE37 records from M1g mooring in 2008–2010, and ADCP records for 2008-2010. This layer is the key part of the lower halocline water (**Fig. 1a,b**) and has sufficient data coverage for the task. All original mooring data were processed to make them comparable. We filtered MMP vertical profiles with a running-mean filter to reduce resolution to 4 m, equivalent to the 2013-2018 ADCP observations. We subsampled ADCP and SBE37 data in time to match coarser MMP temporal resolution. The vertical shear is calculated consistently using gradients over 20 m vertical scale. Reconstruction of the record at the $M1_4$ mooring site in 2013-2018 using MMP data from nearby moorings is described below.

There were no MMP measurements within the 110-140m depth range at the $M1_4$ mooring in 2013-2015 and 2015-2018 (**Table 1**). Records for these years and depth range were reconstructed using weighted interpolated estimates from the neighboring $M1_3$ and $M1_5$ moorings.

Accepted for publication in *Journal of Climate*. DOI 10.1175/JCLI-D-19-0976.1.

This approach is justified by the observed monotonic cross-slope change of current speed from $M1_3$, $M1_4$, and $M1_5$ mooring records for the depth ranges where overlapping data is available for the three moorings (**Fig. A1**). Estimates of buoyancy frequency *N* derived from temperature and salinity provided by these three moorings are statistically indistinguishable (**Fig. A1**).

Multiple regression is used to further validate the use of records from moorings $M1_3$ and $M1_5$ to reconstruct time series of temperature, salinity, and current speed at mooring $M1_4$ for 2013-2018. The model of multiple regression is

$$Y = \beta_o + \beta_1 X_1 + \beta_2 X_2 \,, \qquad (1)$$

where $\beta_1 = \frac{r_{YX_1} - r_{YX_2} r_{X_1X_2}}{1 - r_{X_1X_2}^2} \frac{\sigma_Y}{\sigma_{X_1}}$, $\beta_2 = \frac{r_{YX_2} - r_{YX_1} r_{X_1X_2}}{1 - r_{X_1X_2}^2} \frac{\sigma_Y}{\sigma_{X_2}}$, and $\beta_o = \overline{Y} - \beta_1 \overline{X}_1 + \beta_2 \overline{X}_2$,

overbar denotes means, σ denotes standard deviations, *r* is used to denote cross-correlation coefficients, and random error term is neglected. For independent parameters X_1 and X_2 time series from $M1_3$ and $M1_5$ moorings are used, time series from $M1_4$ is used as the dependent variable *Y*. We neglected the high-frequency part of the records by applying low-pass three-month running mean filtering to each time series used in the tests because in this study we mainly focus on longer-term (interannual) trends and changes. Evidence for the validity of this approach is provided in **Fig. A2**.

Acknowledgments. The ship-based oceanographic observations in the eastern EB and Laptev Sea were conducted under the framework of the NABOS project with support from NSF (grants AON-1203473 and AON-1947162). Analyses presented in this paper are supported by NSF grants 1708427 and 1708424. The contributions from TPR and MAJ were supported by PEANUTS (NE/R01275X/1 and 03F0804A), part of the Changing Arctic Ocean programme,

Accepted for publication in *Journal of Climate*. DOI 10.1175/JCLI-D-19-0976.1.

447 jointly funded by the UKRI Natural Environment Research Council (NERC) and the German
448 Federal Ministry of Education and Research (BMBF). This paper is based in part on ideas
449 discussed at an international workshop on pan-Arctic marine systems in Motovun Croatia,
450 organized by P. Wassmann and supported by funding from Arctic SIZE
451 (http://site.uit.no/arcticsize/). All mooring data used in this study are available at
452 https://arcticdata.io/catalog/#view/arctic-data (doi: 10.18739/A2N37R and
453 10.18739/A2HT2GB80).

454

455

456

Accepted for publication in *Journal of Climate*. DOI 10.1175/JCLI-D-19-0976.1.

References

Barton, B. I., Y.-D. Lenn, and C. Lique, 2018: Observed atlantification of the Barents Sea causes the polar front to limit the expansion of winter sea ice. *J. Phys. Oceanogr*., **48**(8), 1849-1866.

Baumann, T. M., I. V. Polyakov, A. V. Pnyushkov, R. Rember, V. V. Ivanov, M. B. Alkire, I. Goszczko, and E. C. Carmack, 2018: On the seasonal cycles observed at the continental slope of the Eastern Eurasian Basin of the Arctic Ocean. *J. Phys. Oceanogr*., **48**, 1451-1470, DOI: 10.1175/JPO-D-17-0163.1.

Bluhm B. A., K. N. Kosobokoba, and E. C. Carmack, 2015: A tale of two basins: An integrated physics and biology perspective of the deep Arctic Ocean. *Progress in Oceanography* http://dx.doi.org/10.1016/j.pocean.2015.07.011.

Carmack E., I. Polyakov, L. Padman, I. Fer, E. Hunke, J. Hutchings, J. Jackson, D. Kelley, R. Kwok, C. Layton, D. Perovich, O. Persson, B. Ruddick, M.-L. Timmermans, J. Toole, T. Ross, S. Vavrus, and P. Winsor, 2015: The new Arctic: Towards quantifying the increasing role of oceanic heat in sea ice loss, *BAMS*, **96**(12), 2079-2105, 10.1175/BAMS-D-13-00177.1.

Carr, M., P. Sutherland, A. Haase, K.- U. Evers, I. Fer, A. Jensen, H. Kalisch, J. Berntsen, E. Părău, Ø. Thiem and PA. Davies (2019). Laboratory Experiments on Internal Solitary Waves in Ice- Covered Waters. Geophysical Research Letters, 2019GL084710

Cavalieri, D. J., C. L. Parkinson, P. Gloersen, and H. J. Zwally. 1996, updated yearly. *Sea Ice Concentrations from Nimbus-7 SMMR and DMSP SSM/I-SSMIS Passive Microwave Data, Version 1*. Boulder, Colorado USA. NASA National Snow and Ice Data Center Distributed Active Archive Center. doi: https://doi.org/10.5067/8GQ8LZQVL0VL.

Falk-Petersen, S., V. Pavlov, J. Berge, F. Cottier, K. M. Kovacs, and C. Lydersen, 2015: At the rainbow's end: High productivity fueled by winter upwelling along an Arctic shelf. *Polar Biol.*, **38**, 5–11.

Fer, I., 2009: Weak vertical diffusion allows maintenance of cold halocline in the central Arctic. *Atmos. Ocean. Sci. Lett.*, **2**, 148-152.

Accepted for publication in *Journal of Climate*. DOI 10.1175/JCLI-D-19-0976.1.

485 Fer, I., R. Skogseth, and F. Geyer, 2010: Internal waves and mixing in the Marginal Ice Zone
486 near the Yermak Plateau. *J. Phys. Oceanogr*. **40**(7), 1613-1630. doi:
487 10.1175/2010JPO4371.1.
488 Frances, J. A., S. J. Vavrus, and J. Cohen, 2017: Amplified actic warming and mid-latitude
489 weather: new perspectives on emerging connections. *Wiley Interdisciplinary Reviews:*
490 *Climate Change*, **8**(5), e474.
491 Garcia- Serrano, J., C. Frankignoul, G. Gastineau, and A. de la Camera, 2015: On the
492 predictability of the winter euro-atlantic climate: lagged influence of autumn arctic sea
493 ice. *J. Clim*., **28**(13), 5195-5216.
494 Graham, R. M., *et al*., 2019: Winter storms accelerate the demise of sea ice in the Atlantic sector
495 of the Arctic Ocean, *Scientific Reports*, **9**, 9222, 10.1038/s41598-019-45574-5.
496 Kelley, D., 1984. Effective diffusivities within oceanic thermohaline staircases. *J. Geophys.*
497 *Res.: Oceans*, **89**(C6), 10484-10488.
498 Kolstad, E., and J. Screen, 2019: Non-stationary relationship between autumn arctic sea ice and
499 the winter north atlantic oscillation, *Geophys. Res. Lett*., **46**(13), 7583-7591.
500 Kwok, R., 2018: Arctic sea ice thickness, volume, and multiyear ice coverage: losses and
501 coupled variability (1958–2018), *Environ. Res. Lett.* **13**, 105005.
502 Lenn, Y.-D., P. Wiles, S. Torres-Valdes, E. Abrahamsen, T. Rippeth, J. H. Simpson, S. Bacon, S.
503 Laxon, I. Polyakov, V. Ivanov, and S. Kirillov, 2009: Vertical mixing at intermediate
504 depths in the Arctic boundary current, *Geophys. Res. Lett*., **36**, L05601, doi:
505 10.1029/2008GL036792.
506 Lind, S., R. B. Ingvaldsen, and T. Furevik, 2018: Declining sea ice import and freshwater loss
507 causes Arctic warming hotspot. *Nature Climate Change*, **8**(7), doi:10.1038/s41558-018-
508 0205-y.
509 Manabe, S., and R. J. Stouffer, 1980: Sensitivity of a global climate model to an increase of CO2
510 concentration in the atmosphere. *J. Geophys. Res*., **85**, 5529-5554.

Accepted for publication in *Journal of Climate*. DOI 10.1175/JCLI-D-19-0976.1.

Onarheim, I. H., T. Eldevik, L. H. Smedsrud, and J. C. Stroeve, 2018: Seasonal and regional manifestation of Arctic sea ice loss. *J. Climate*, **31**, 4917-4932, DOI: 10.1175/JCLI-D-17-0427.1.

Perovich, D. K., J. A. Richter-Menge, K. F. Jones, and B. Light, 2008: Sunlight, water, and ice: Extreme Arctic sea ice melt during the summer of 2007, *Geophys. Res. Lett*., **35**, L11501, doi:10.1029/2008GL034007.

Polyakov, I. V., A. Beszczynska, E. C. Carmack, I. A. Dmitrenko, E. Fahrbach, I. E. Frolov, R. Gerdes, E. Hansen, J. Holfort, V. V. Ivanov, M. A. Johnson, M. Karcher, F. Kauker, J. Morison, K. A. Orvik, U. Schauer, H. L. Simmons, Ø. Skagseth, V. T. Sokolov, M. Steele, L. A. Timokhov, D. Walsh, and J. E. Walsh, 2005: One more step toward a warmer Arctic. *Geophys. Res. Lett*., **32**, L17605, doi:10.1029/2005GL023740.

Polyakov, I. V., L. A. Timokhov, V. A. Alexeev, S. Bacon, I. A. Dmitrenko, L. Fortier, I. E. Frolov, J.-C. Gascard, E. Hansen, V. V. Ivanov, S. Laxon, C. Mauritzen, D. Perovich, K. Shimada, H. L. Simmons, V. T. Sokolov, M. Steele, and J. Toole, 2010: Arctic Ocean warming reduces polar ice cap, *J. Phys. Oceanogr.*, DOI: 10.1175/2010JPO4339.1, **40**, 2743–2756.

Polyakov, I. V., A. V. Pnyushkov, R. Rember, L. Padman, E. C. Carmack, and J. Jackson, 2013: Winter convection transports Atlantic Water heat to the surface layer in the eastern Arctic Ocean, *J. Phys. Oceanogr*., **43**(10), 2148–2162, DOI: 10.1175/JPO-D-12-0169.1.

Polyakov, I. V., A. V. Pnyushkov, M. Alkire, I. M. Ashik, T. Baumann, E. Carmack, I. Goszczko, V. Ivanov, T. Kanzow, R. Krishfield, R. Kwok, A. Sundfjord, J. Morison, R. Rember, and A. Yulin, 2017: Greater role for Atlantic inflows on sea-ice loss in the Eurasian Basin of the Arctic Ocean, *Science*, **356**(6335), 285-291, doi: 10.1126/science.aai8204.

Polyakov, I. V., A. V. Pnyushkov, and E. C. Carmack, 2018: Stability of the arctic halocline: A new indicator of arctic climate change. *Environ. Res. Letts*., **13**, 125008, https://doi.org/10.1088/1748-9326/aaec1e.

Polyakov, I. V., L. Padman, Y.-D. Lenn, A. V. Pnyushkov, R. Rember and V. V. Ivanov, 2019: Eastern Arctic Ocean diapycnal heat fluxes through large double-diffusive steps, *J. Phys. Oceanogr*., **49**, 227-246, DOI: 10.1175/JPO-D-18-0080.1.

Accepted for publication in *Journal of Climate*. DOI 10.1175/JCLI-D-19-0976.1.

Polyakov, I. V., M. B. Alkire, B. A. Bluhm, K. Brown, E. C. Carmack, M. Chierici, S. Danielson, I. Ellingsen, E. A. Ershova, K. Gårdfeldt, R. B. Ingvaldsen, A. V. Pnyushkov, D. Slagstad, P. Wassmann, 2020a: Borealization of the Arctic Ocean in response to anomalous advection from sub-arctic seas, *Frontiers in Marine Science*. Submitted.

Polyakov, I. V., T. P. Rippeth, I. Fer, T. M. Baumann, E. C. Carmack, V. V. Ivanov, M. Janout, L. Padman, A. V. Pnyushkov, and R. Rember, 2020b: Transition to a new ocean dynamic regime in the eastern Arctic Ocean. *Geophys. Res. Lett.* Submitted.

Pnyushkov, A., Polyakov, I., Ivanov, V., Aksenov, Ye., Coward, A., Janout, M., and Rabe , B. 2015: Structure and variability of the boundary current in the Eurasian Basin of the Arctic Ocean. *Deep-Sea Res.-I,* **101**(7), p.80-97, doi:10.1016/j.dsr.2015.03.001.

Pnyushkov, A. V., I. V. Polyakov, R. Rember, V. V. Ivanov, M. B. Alkire, I. M. Ashik, T. M. Baumann, G. V. Alekseev, and A. Sundfjord, 2018: Heat, salt, and volume transports in the eastern Eurasian Basin of the Arctic Ocean from 2 years of mooring observations. *Ocean Sci*., **14**, 1349-1371, https://doi.org/10.5194/os-14-1349-2018.

Pnyushkov, A., Polyakov, I. V., Padman, L., and Nguyen, A. T. 2018b: Structure and dynamics of mesoscale eddies over the Laptev Sea continental slope in the Arctic Ocean, *Ocean Sci*., **14**, 1329-1347, https://doi.org/10.5194/os-14-1329-2018.

Provost, C., Sennechael, N., Miguet, J., Itkin, P., Rosel, A., Koenig, Z., Villacieros-Robineau, N., and M. A. Granskog, 2017: Observations of flooding and snow-ice formation in a thinner Arctic sea-ice regime during the N-ICE2015 campaign: Influence of basal ice melt and storms, *J. Geophys. Res. Oceans*, **122**, 7115–7134, doi:10.1002/2016JC012011.

Renner, A. H. H., Sundfjord, A., Janout, M. A., Ingvaldsen, R., Beszczynska-Möller, A., Pickart, R., and Pérez-Hernández, M., (2018). Variability and redistribution of heat in the Atlantic Water boundary current north of Svalbard. *J. Geophys. Res.: Oceans*, **123**, 6373–6391. https://doi.org/10.1029/2018JC013814

Rippeth, T. P., Lincoln, B. J., Lenn, Y.-D., Green, J. M., Sundfjord, A., and Bacon, S. 2015: Tide-mediated warming of Arctic halocline by Atlantic heat fluxes over rough topography. *Nature Geosci.* **8**, 191–194, doi:10.1038/ngeo2350.

Accepted for publication in *Journal of Climate*. DOI 10.1175/JCLI-D-19-0976.1.

568 Shibley, N. C., M.-L. Timmermans, J. R. Carpenter, and J. M. Toole, 2017: Spatial variability of
569 the Arctic Ocean's double-diffusive staircase, *J. Geophys. Res. Oceans*, **122**, 980-994,
570 doi:10.1002/2016JC012419.

571 Silvester, J. M., Y.D. Lenn, J.A. Polton, T.P. Rippeth & M.M. Maqueda, M. M. (2014).
572 Observations of a diapycnal shortcut to adiabatic upwelling of Antarctic Circumpolar Deep
573 Water. *Geophys. Res. Lett.*, **41**, 7950-7956.

574 Steele, M., and T. Boyd, 1998: Retreat of the cold halocline layer in the Arctic Ocean. *J.*
575 *Geophys. Res. - Oceans*., **103**(C5), 10419-10435.

576 Stroeve, J., and D. Notz, 2018: Changing state of Arctic sea ice across all seasons. *Env. Res.*
577 *Lett*., **13**, 103001.

578 Timmermans, M.-L., J. Toole, and R. Krishfield, 2018: Warming of the interior Arctic Ocean
579 linked to sea ice losses at the basin margins. *Science Advances*, **4**: eaat6773.

580 Toole, J. M., M. L. Timmermans, D. K. Perovich, R. A. Krishfield, A. Proshutinsky, and J. A.
581 Richter-Menge, 2010: Influences of the ocean surface mixed layer and thermohaline
582 stratification on Arctic Sea ice in the central Canada Basin. *J. Geophys. Res*., **115,** C10018,
583 doi:10.1029/2009jc005660.

584 Torrence, C. and G. P. Compo, 1998: A practical guide to wavelet analysis. *Bull. Amer. Meteor.*
585 *Soc.* **79**(1), 61-78.

586

Accepted for publication in *Journal of Climate*. DOI 10.1175/JCLI-D-19-0976.1.

Figure legends

Figure 1: Vertical profiles of (a) potential temperature θ, (b) salinity S, (c) the logarithm of squared Brunt-Väisälä frequency (N^2, s^{-2}, a measure of water column stability; 5-point smoothing is applied) and (d) nutrients at $M1_4$ mooring site made on August 27, 2013, September 20, 2015, and September 2, 2018. Circulation of the intermediate Atlantic Water (AW) in the Arctic Ocean is shown schematically in (e) by red arrows. In (a), the upper part of halocline is cold halocline layer (CHL) in which salinity increases with depth while temperature remains near the freezing point. The blue box indicates the area of the Arctic Ocean with mooring positions shown in **Fig. 2**. The Canada Basin (CB), Chukchi Sea (CS), East Siberian Sea (ESS), and Barents Sea (BS) are indicated.

Figure 2: Map showing the focus of the study together with the positions of moorings and location of CTD (Conductivity-Temperature-Depth) profiles made in summer 2013, 2015, and 2018 reported in this study. The Gakkel Ridge (GR) divides the Eurasian Basin (EB) into the Nansen Basin and the Amundsen Basin. The Lomonosov Ridge (LR), Novosibirskiye Islands (NI), Severnaya Zemlya (SZ), Franz Joseph Land (FJL), and Makarov Basin (MB) are indicated. Grey solid lines show depth in meters. The eastern EB region used for calculation of blue time series in **Fig. 10** is identified by green line.

Figure 3: Composite 2002 –2018 time series of (a) monthly mean potential water temperature (θ) and (c) daily depth of the lower halocline boundary (H_{base}) defined by 0°C isotherm at $M1_4$ mooring location (for location, see **Fig. 2**). (b) Comparison of de-seasoned monthly mean time series of normalized θ anomalies from 250m of M14 mooring of the eastern EB (EEB) and lagged by 678 days (as obtained from correlation analysis) F2-F3 moorings of Fram Strait; time series are normalized by their standard deviations.

Figure 4: Depth–time diagram of potential temperature θ (°C) from $M1_3$ mooring. Black lines show the depth of the halocline base and lower Atlantic Water boundary both defined by 0°C isotherms.

Figure 5: Estimates of (left) annual and (right) summer mean (a,b) squared buoyancy frequency N^2 (10^5 s^{-2}), (c,d) current magnitude $|\mathbf{U}|$ and squared vertical shear of horizontal currents $|\mathbf{U}_z|^2$, and (e,f) proxy of Richardson number Ri for the 110-140 m depth range for the $M1_4$ mooring location. Statistical significance of means is shown at the 95% confidence level.

Accepted for publication in *Journal of Climate*. DOI 10.1175/JCLI-D-19-0976.1.

Figure 6: (Left and middle) 65-140m layer depth versus time of water temperature and annual component of heat content Q. Annual components are obtained via band-pass filtering using wavelet transformations. Horizontal black segments identify the depth of seasonal ventilation; dates identified by their ends are used to compute vertically integrated Q shown in the lower parts of panels in the right column. (Right) Vertically integrated Q for the beginning (warm phase) and end (cold phase) of seasonal ventilation (lower parts of the panels) and divergent heat fluxes δF_h (upper parts) for four moorings.

Figure 7: Time-averaged over M3, $M1_2$, $M1_3$, and $M1_4$ mooring records (top) vertically integrated Q for the beginning (warm phase, red bars, Q_{max}) and end (cold phase, blue bars, Q_{min}) of seasonal ventilation of eastern EB halocline (110-140m), (middle) divergent heat fluxes δF_h (blue bars for averages with ±1 standard error shown as black segments), and (bottom) equivalent sea ice thickness losses.

Figure 8: (a) Potential temperature, (b) annual component of heat content Q obtained by band-pass filtering of daily heat content using wavelet spectra; horizontal black segments identify the depth of seasonal ventilation, (c) salinity, and (d) squared buoyancy frequency for $M1_3$ mooring.

Figure 9: (left) Depth versus time diagram of potential water temperature θ (^{o}C) and (right) time series of monthly heat content Q for the 65-140m layer (blue) and AW core temperature (red) for four moorings. Low correlations between these time series $R_{Q\text{-}\theta}$ suggest that changes of Q are not related to seasonal shift of AW core relative to the slope.

Figure 10: Normalized (reduced to anomalies and divided by one standard deviation SD) annual time series of (blue) halocline salinity S in the eastern EB (EEB, from Polyakov et al. 2018) and (red) lagged by one year (as obtained from correlation analysis) upper ocean S from the northern Barents Sea (from Lind et al. 2018). Dash-dotted lines are used to fill gaps (interpolated values are *not* used for statistical estimates). Means and SDs are indicated. Trends are shown by dashed lines; all trends are statistically significant at the 95% confidence according to the Student t test. The break-point in 1999 separates periods with opposite trends.

Figure 11: Conceptual model of shift of the mixing regime in the eastern EB in recent years and associated suite of processes and state conditions including: 1) thinner, more mobile ice, 2) warmer surface mixed layer (SML), 3) weakening / retreat of cold halocline (HC) layer, 4) increased AW vertical heat flux (red arrows) and horizontal currents and their vertical shear

Accepted for publication in *Journal of Climate*. DOI 10.1175/JCLI-D-19-0976.1.

(blue arrows), 5) shoaling of upper AW boundary, and 6) replacement of DD by shear instabilities as the fundamental mechanism of vertical flux.

Figure A1: 2013/15 mean estimates of (top) squared Brunt-Väisälä frequency N^2, and current speed |**U**| for (middle) 20-60 m and (bottom) 190-230 m depth ranges where the mooring records from $M1_3$, $M1_4$, and $M1_5$ overlap. Statistical significance of estimates for means is shown at the 95% confidence level.

Figure A2: Multiple regression reconstruction of (a,b) salinity and (c,d) current speed |**U**| at $M1_4$ mooring site using data from $M1_3$ and $M1_5$ moorings for 170-210m depth range. (a,c) Daily (dotted) and three-month running mean smoothed time series of (a) salinity and (c) |**U**| from $M1_3$, $M1_4$, and $M1_5$ moorings. (b,d) Original (blue) and reconstructed (red) time series of (b) salinity and (d) |**U**| from $M1_4$ mooring. Relatively high correlations between the original and reconstructed time series attests of good quality of reconstruction.

Figures

Accepted for publication in *Journal of Climate*. DOI 10.1175/JCLI-D-19-0976.1.

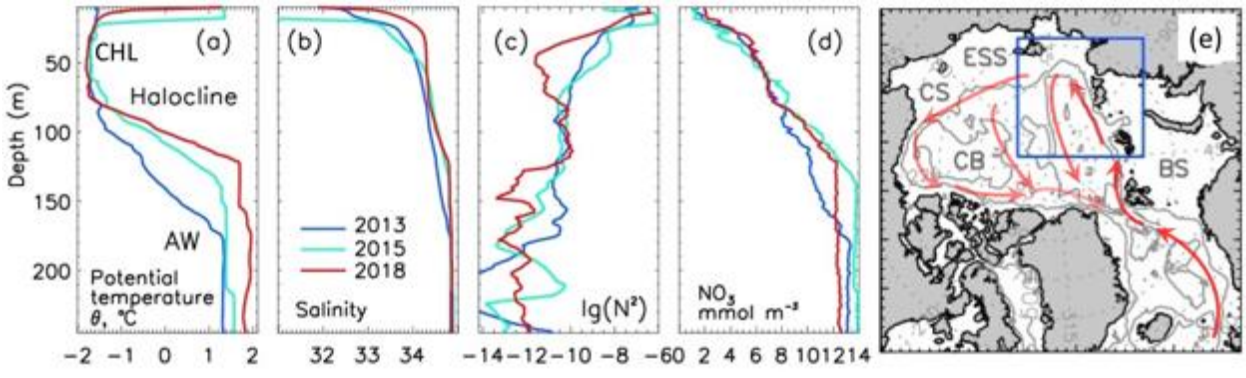

Figure 1: Vertical profiles of (a) potential temperature θ, (b) salinity S, (c) the logarithm of squared Brunt-Väisälä frequency (N^2, s^{-2}, a measure of water column stability; 5-point smoothing is applied) and (d) nutrients at $M1_4$ mooring site made on August 27, 2013, September 20, 2015, and September 2, 2018. Circulation of the intermediate Atlantic Water (AW) in the Arctic Ocean is shown schematically in (e) by red arrows. In (a), the upper part of halocline is cold halocline layer (CHL) in which salinity increases with depth while temperature remains near the freezing point. The blue box indicates the area of the Arctic Ocean with mooring positions shown in **Fig. 2**. The Canada Basin (CB), Chukchi Sea (CS), East Siberian Sea (ESS), and Barents Sea (BS) are indicated.

Accepted for publication in *Journal of Climate*. DOI 10.1175/JCLI-D-19-0976.1.

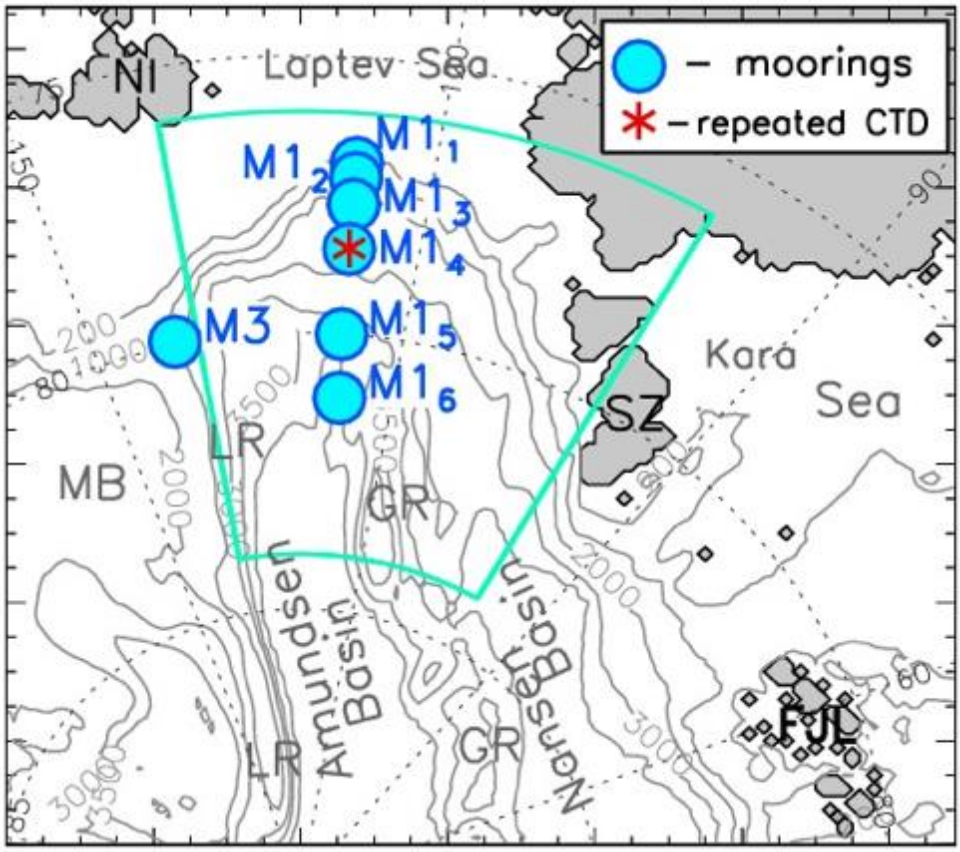

687

688 **Figure 2**: Map showing the focus of the study together with the positions of moorings and location
689 of CTD (Conductivity-Temperature-Depth) profiles made in summer 2013, 2015, and 2018
690 reported in this study. The Gakkel Ridge (GR) divides the Eurasian Basin (EB) into the Nansen
691 Basin and the Amundsen Basin. The Lomonosov Ridge (LR), Novosibirskiye Islands (NI),
692 Severnaya Zemlya (SZ), Franz Joseph Land (FJL), and Makarov Basin (MB) are indicated. Grey
693 solid lines show depth in meters. The eastern EB region used for calculation of blue time series in
694 **Fig. 10** is identified by green line.

695

696

Accepted for publication in *Journal of Climate*. DOI 10.1175/JCLI-D-19-0976.1.

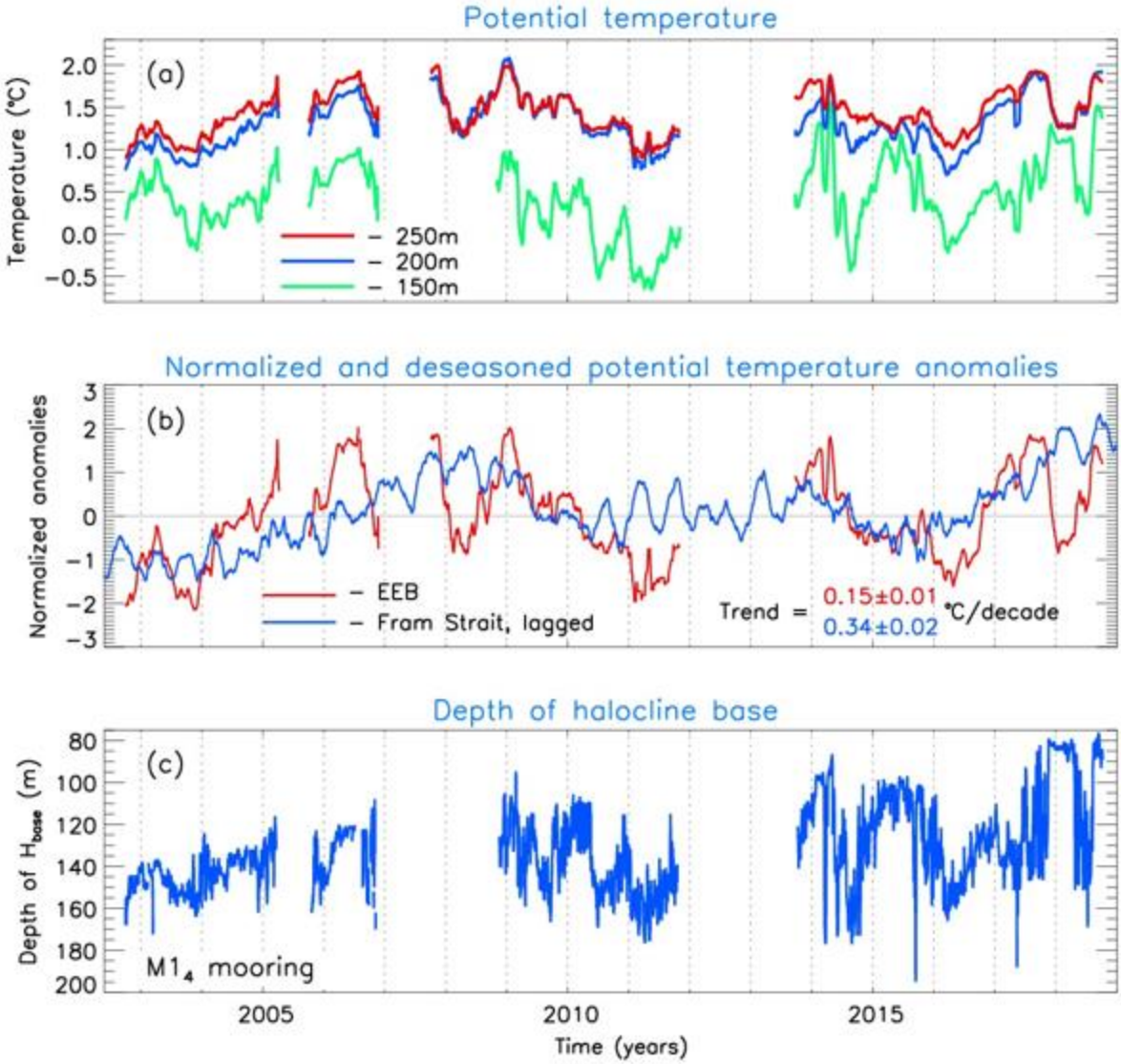

Figure 3: Composite 2002 –2018 time series of (a) monthly mean potential water temperature (θ) and (c) daily depth of the lower halocline boundary (H_{base}) defined by 0°C isotherm at M1$_4$ mooring location (for location, see **Fig. 2**). (b) Comparison of de-seasoned monthly mean time series of normalized θ anomalies from 250m of M14 mooring of the eastern EB (EEB) and lagged by 678 days (as obtained from correlation analysis) F2-F3 moorings of Fram Strait; time series are normalized by their standard deviations.

Accepted for publication in *Journal of Climate*. DOI 10.1175/JCLI-D-19-0976.1.

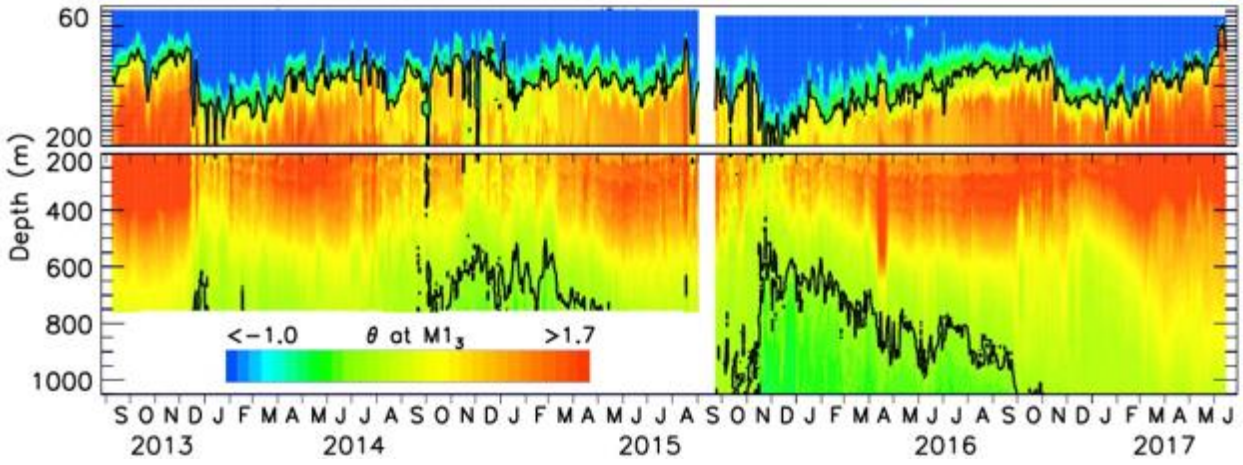

704

705 **Figure 4**: Depth–time diagram of potential temperature θ (°C) from $M1_3$ mooring. Black lines
706 show the depth of the halocline base and lower Atlantic Water boundary both defined by 0°C
707 isotherms.

708

Accepted for publication in *Journal of Climate*. DOI 10.1175/JCLI-D-19-0976.1.

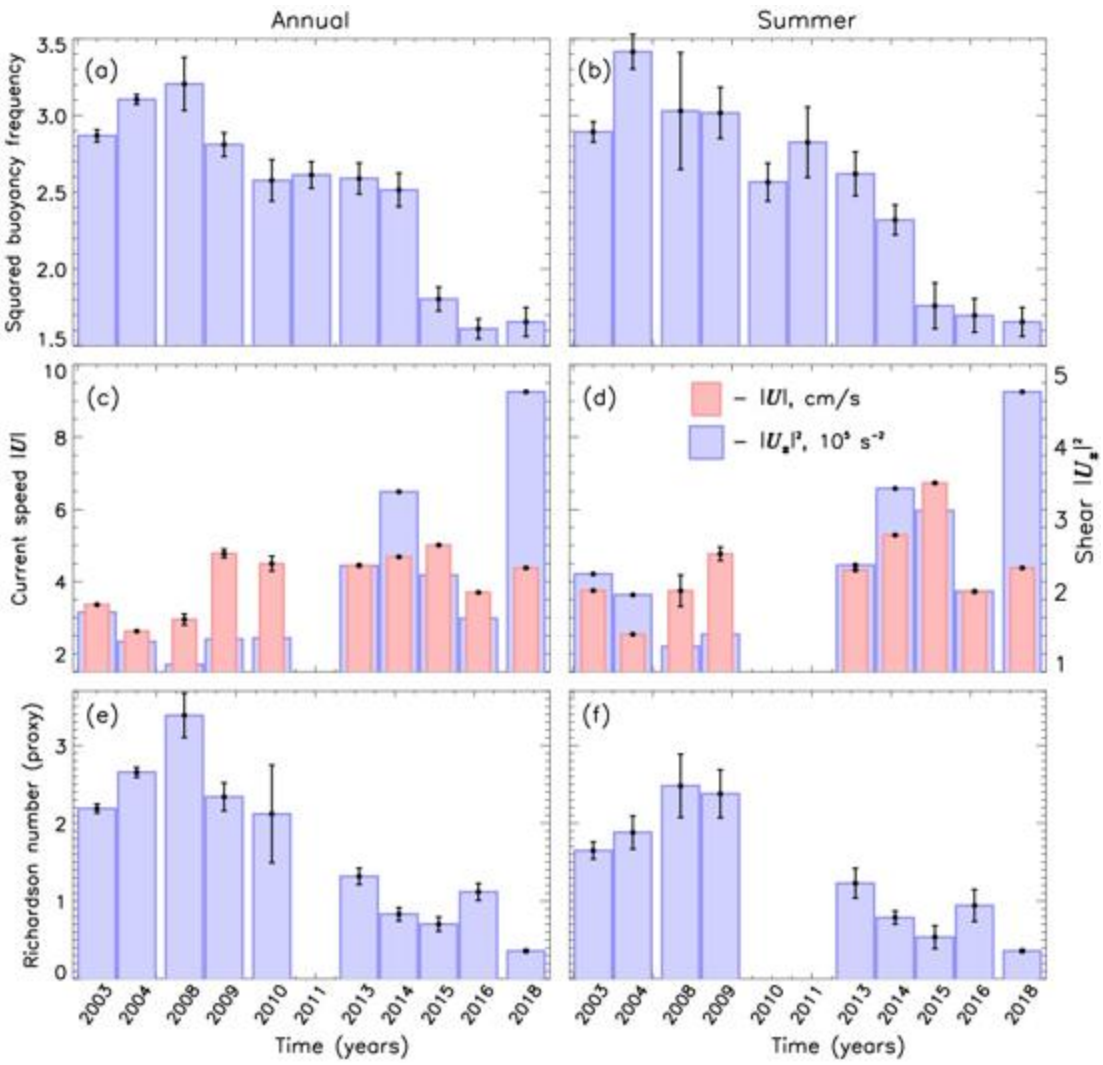

Figure 5: Estimates of (left) annual and (right) summer mean (a,b) squared buoyancy frequency N^2 (10^5 s^{-2}), (c,d) current magnitude $|\mathbf{U}|$ and squared vertical shear of horizontal currents $|\mathbf{U}_z|^2$, and (e,f) proxy of Richardson number *Ri* for the 110-140 m depth range for the $M1_4$ mooring location. Statistical significance of means is shown at the 95% confidence level.

Accepted for publication in *Journal of Climate*. DOI 10.1175/JCLI-D-19-0976.1.

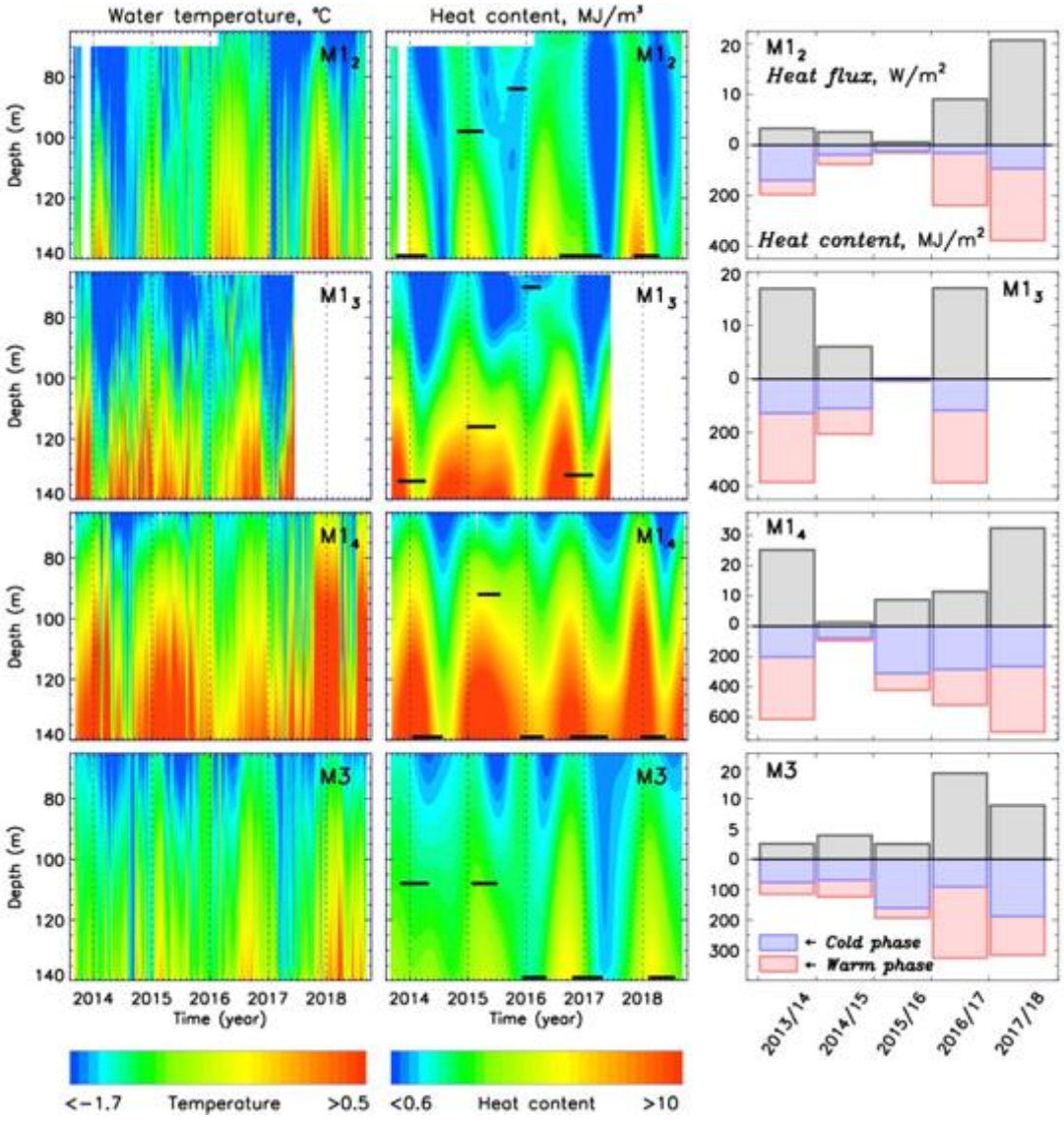

Figure 6: (Left and middle) 65-140m layer depth versus time of water temperature and annual component of heat content Q. Annual components are obtained via band-pass filtering using wavelet transformations. Horizontal black segments identify the depth of seasonal ventilation; dates identified by their ends are used to compute vertically integrated Q shown in the lower parts of panels in the right column. (Right) Vertically integrated Q for the beginning (warm phase) and end (cold phase) of seasonal ventilation (lower parts of the panels) and divergent heat fluxes δF_h (upper parts) for four moorings.

Accepted for publication in *Journal of Climate*. DOI 10.1175/JCLI-D-19-0976.1.

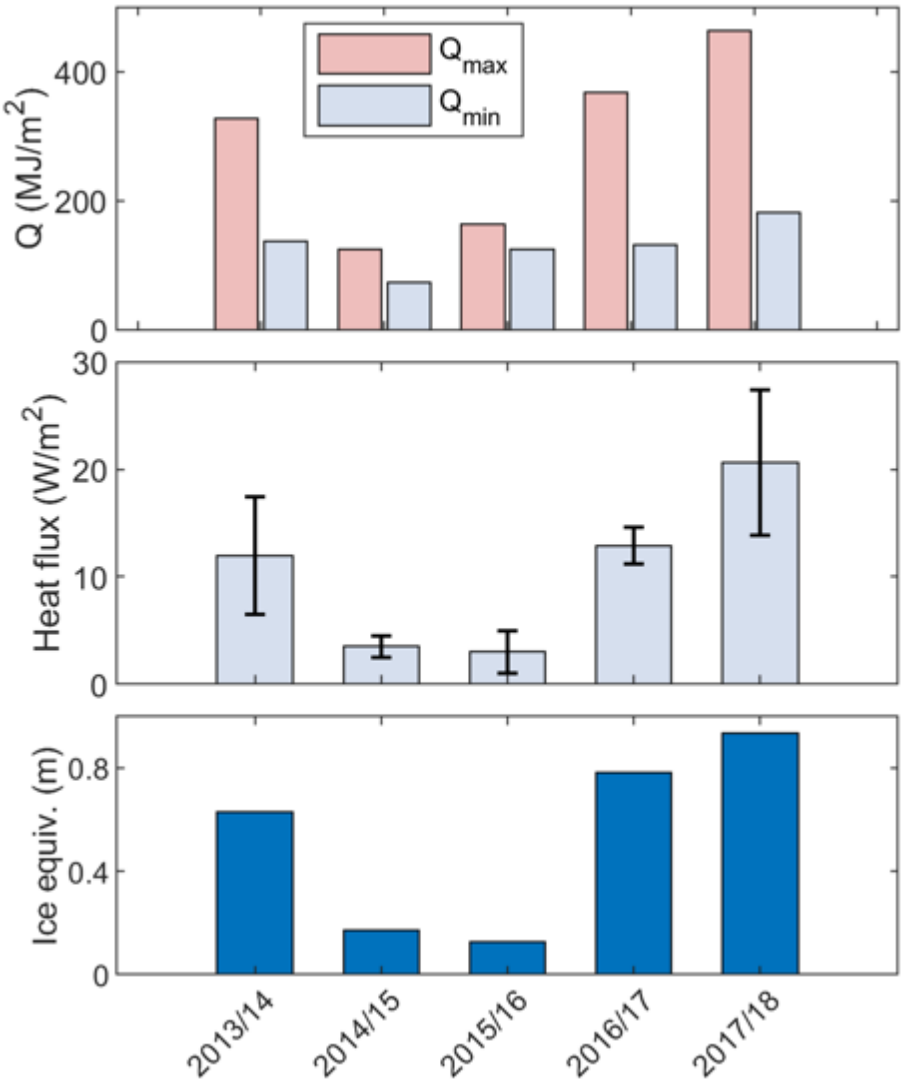

725
726

727 **Figure 7**: Time-averaged over M3, $M1_2$, $M1_3$, and $M1_4$ mooring records (top) vertically
728 integrated Q for the beginning (warm phase, red bars, Q_{max}) and end (cold phase, blue bars, Q_{min})
729 of seasonal ventilation of eastern EB halocline (110-140m), (middle) divergent heat fluxes δF_h
730 (blue bars for averages with ±1 standard error shown as black segments), and (bottom) equivalent
731 sea ice thickness losses.

Accepted for publication in *Journal of Climate*. DOI 10.1175/JCLI-D-19-0976.1.

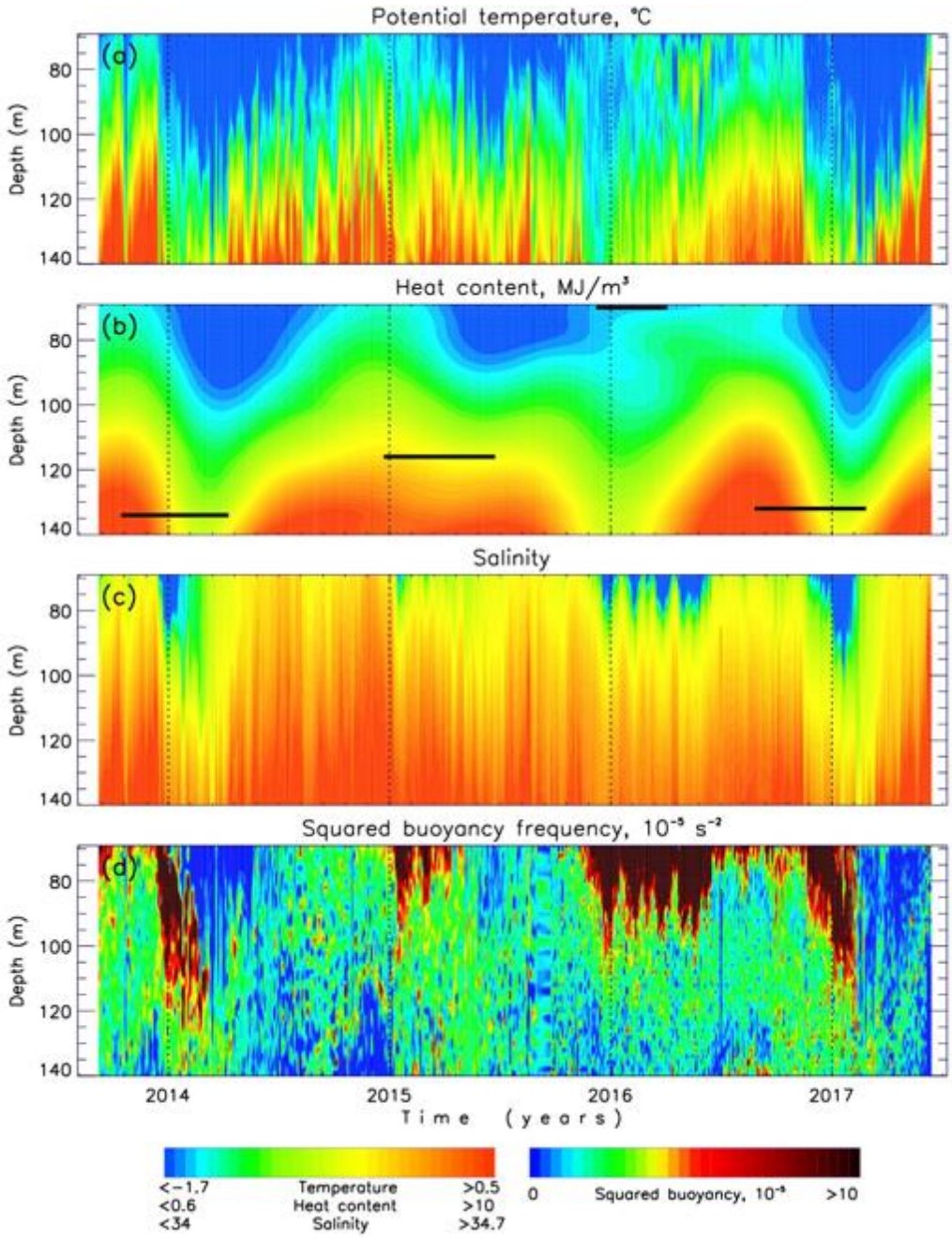

732

733 **Figure 8**: (a) Potential temperature, (b) annual component of heat content *Q* obtained by band-
734 pass filtering of daily heat content using wavelet spectra; horizontal black segments identify the
735 depth of seasonal ventilation, (c) salinity, and (d) squared buoyancy frequency for $M1_3$ mooring.

Accepted for publication in *Journal of Climate*. DOI 10.1175/JCLI-D-19-0976.1.

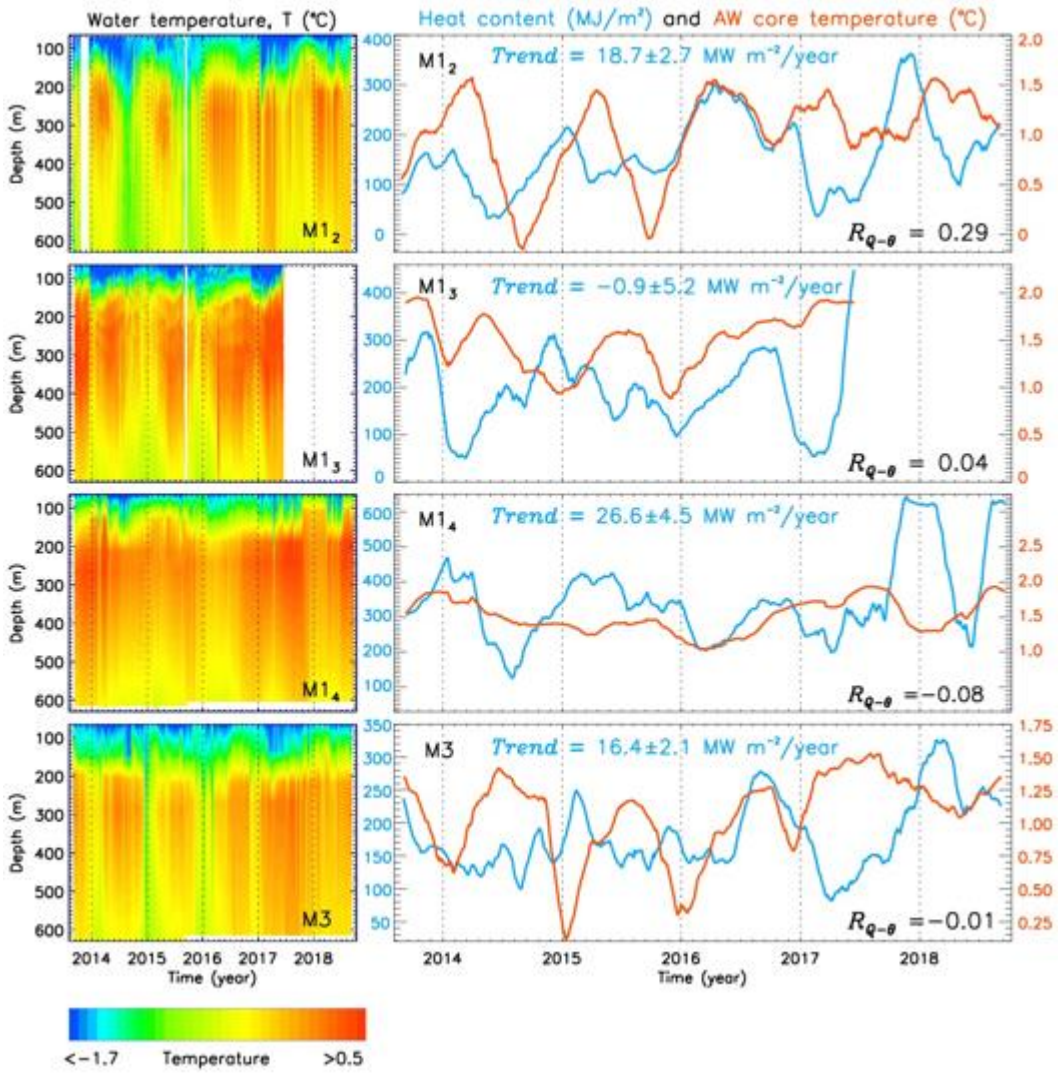

736

737 **Figure 9**: (left) Depth versus time diagram of potential water temperature θ (°C) and (right) time
738 series of monthly heat content Q for the 65-140m layer (blue) and AW core temperature (red) for
739 four moorings. Low correlations between these time series $R_{Q\text{-}\theta}$ suggest that changes of Q are not
740 related to seasonal shift of AW core relative to the slope.

741

742

743

744

Accepted for publication in *Journal of Climate*. DOI 10.1175/JCLI-D-19-0976.1.

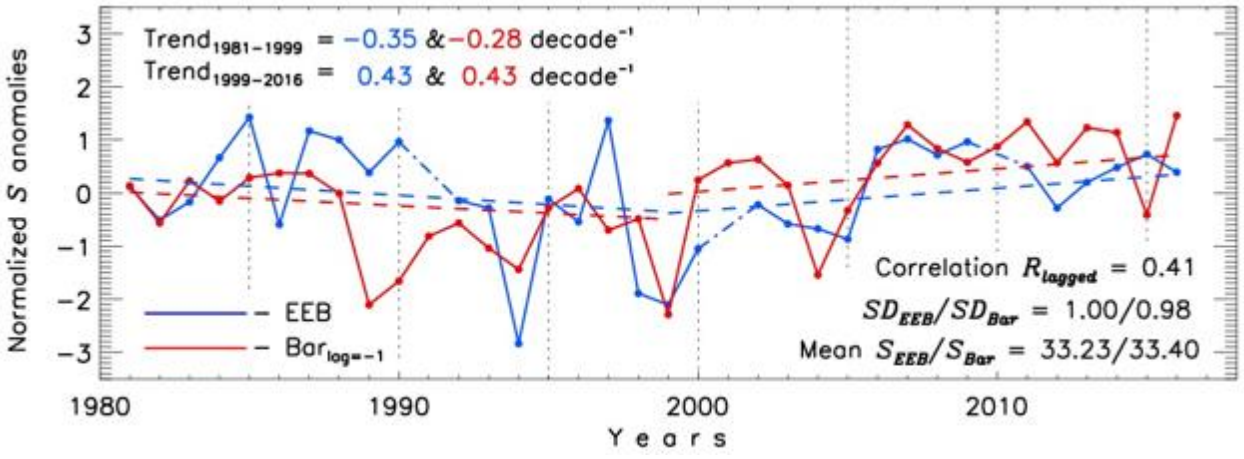

745

746 **Figure 10**: Normalized (reduced to anomalies and divided by one standard deviation SD) annual
747 time series of (blue) halocline salinity *S* in the eastern EB (EEB, from Polyakov et al. 2018) and
748 (red) lagged by one year (as obtained from correlation analysis) upper ocean *S* from the northern
749 Barents Sea (from Lind et al. 2018). Dash-dotted lines are used to fill gaps (interpolated values
750 are *not* used for statistical estimates). Means and SDs are indicated. Trends are shown by dashed
751 lines; all trends are statistically significant at the 95% confidence according to the Student *t* test.
752 The break-point in 1999 separates periods with opposite trends.

753

Accepted for publication in *Journal of Climate*. DOI 10.1175/JCLI-D-19-0976.1.

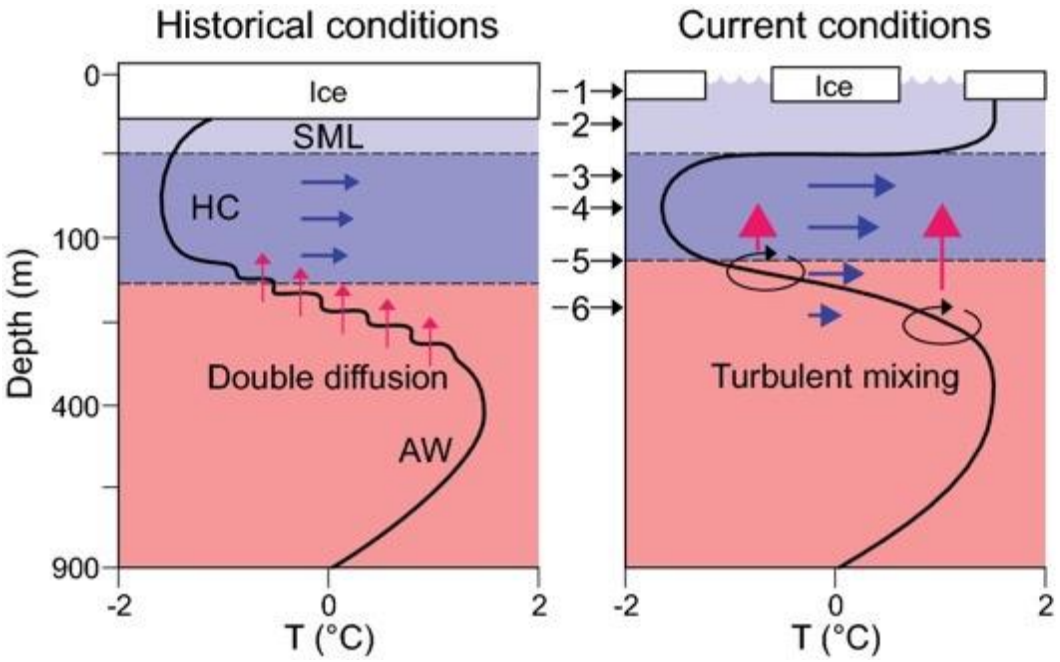

Figure 11: Conceptual model of shift of the mixing regime in the eastern EB in recent years and associated suite of processes and state conditions including: 1) thinner, more mobile ice, 2) warmer surface mixed layer (SML), 3) weakening / retreat of cold halocline (HC) layer, 4) increased AW vertical heat flux (red arrows) and horizontal currents and their vertical shear (blue arrows), 5) shoaling of upper AW boundary, and 6) replacement of DD by shear instabilities as the fundamental mechanism of vertical flux.

Accepted for publication in *Journal of Climate*. DOI 10.1175/JCLI-D-19-0976.1.

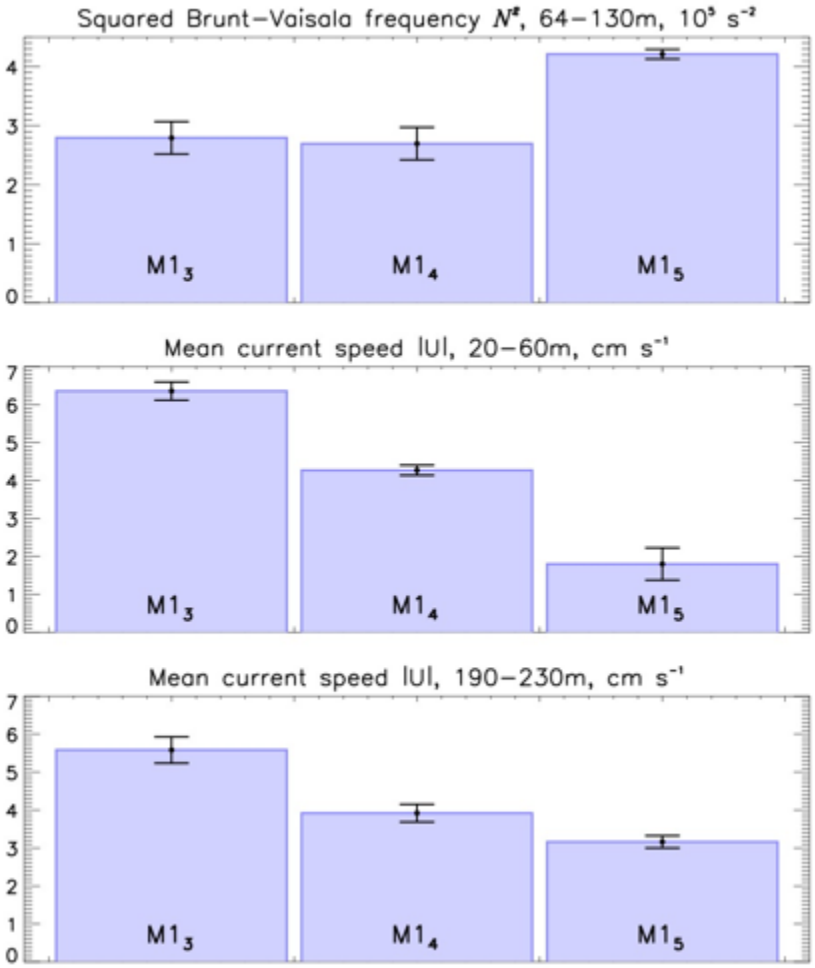

761

762 **Figure A1**: 2013/15 mean estimates of (top) squared Brunt-Väisälä frequency N^2, and current
763 speed |**U**| for (middle) 20-60 m and (bottom) 190-230 m depth ranges where the mooring records
764 from M1$_3$, M1$_4$, and M1$_5$ overlap. Statistical significance of estimates for means is shown at the
765 95% confidence level.

Accepted for publication in *Journal of Climate*. DOI 10.1175/JCLI-D-19-0976.1.

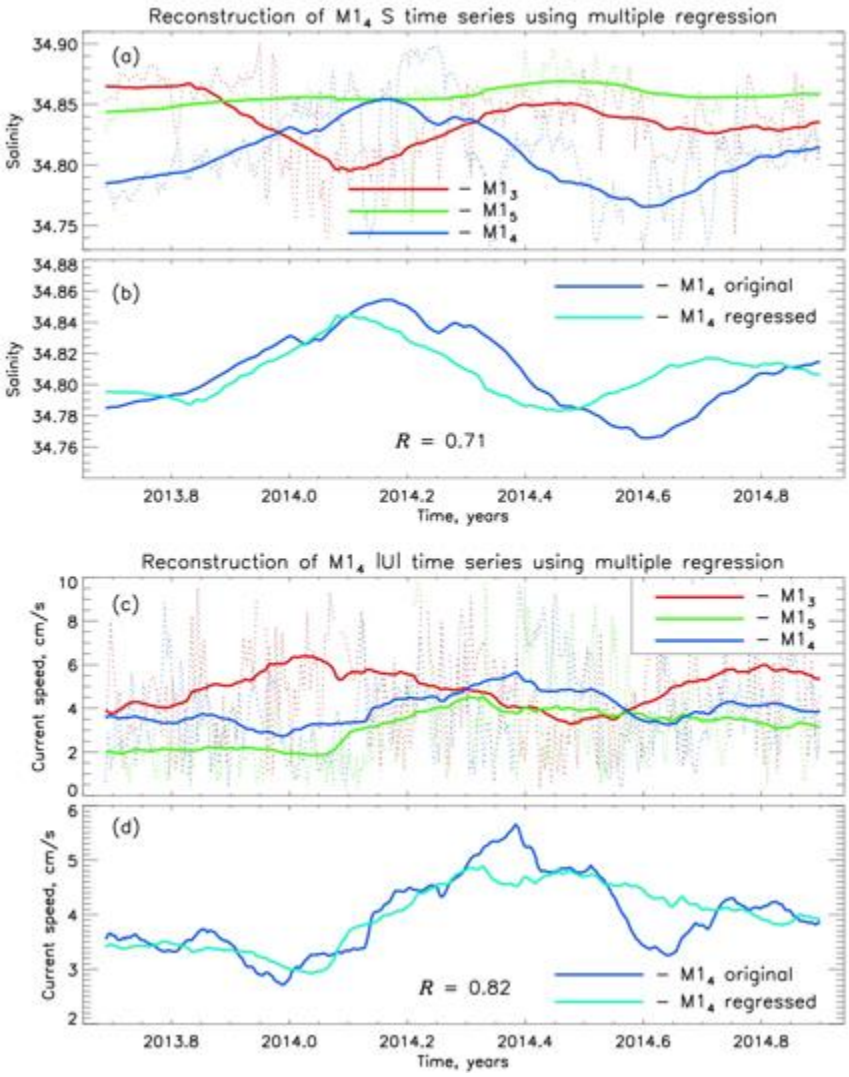

Figure A2: Multiple regression reconstruction of (a,b) salinity and (c,d) current speed |**U**| at M1$_4$ mooring site using data from M1$_3$ and M1$_5$ moorings for 170-210m depth range. (a,c) Daily (dotted) and three-month running mean smoothed time series of (a) salinity and (c) |**U**| from M1$_3$, M1$_4$, and M1$_5$ moorings. (b,d) Original (blue) and reconstructed (red) time series of (b) salinity and (d) |**U**| from M1$_4$ mooring. Relatively high correlations between the original and reconstructed time series attests of good quality of reconstruction.

Accepted for publication in *Journal of Climate*. DOI 10.1175/JCLI-D-19-0976.1.

774 **Table 1:** Summary of deep-water moorings used in this study (only those instruments are shown
775 which records have been used here). For mooring locations, see **Fig. 2**.

Mooring	Latitude (N) Longitute (E)	Depth (m)	Instrument	Depth range (m)	Beginning of record	End of record
Moorings deployed in 2002/09 and collocated with $M1_4$ mooring						
M1a	78 27.360 125 40.440	2680	MMP SBE37	164 –2598 57, 136	09/02/2002	09/01/2003
M1b	78 26.637 125 40.194	2686	MMP	104 –1484	09/08/2003	09/09/2004
M1c	78 26.637 125 40.194	2690	ADCP MMP	5 – 50 72 – 900	09/14/2004 09/15/2004	09/15/2005 07/16/2005
M1e	78 25.940 125 43.419	2692	ADCP MMP	5 – 57 70 – 900	09/02/2006	09/18/2007 10/11/2006
M1g	78 25.735 125 28.527	2765	ADCP SBE37	20 – 130 110, 116, 132, 339	10/18/2008 10/19/2008	06/16/2010 09/22/2011
Mooring section $M1_1$ – $M1_6$, 2013/15						
$M1_1$	77 04.252 125 48.288	250	ADCP	20 – 250	08/26/2013	09/10/2015
$M1_2$	77 10.376 125 47.516	787	ADCP MMP	5 – 63 70 – 754	10/27/2013 08/26/2013	09/01/2015 08/31/2015
$M1_3$	77 39.286 125 48.401	1849	ADCP MMP	5 – 56 64 – 750	09/06/2013 09/07/2013	09/02/2015 09/03/2015
$M1_4$	78 27.543 125 53.758	2721	ADCP ADCP SBE37	5 – 55 193 – 463 62, 129, 214, 265, 617	09/05/2013	09/19/2015
$M1_5$	80 00.199 125 59.673	3443	ADCP MMP	23 – 83 88 – 754	08/28/2013	06/16/2014 08/21/2015
$M1_6$	81 08.182 125 42.673	3900	ADCP MMP	5 – 55 60 – 754	08/29/2013	09/04/2015 08/22/2015
Mooring section $M1_1$ – $M1_5$, 2015/18						
$M1_1$	77 04.221 125 49.577	252	ADCP	200 – 232	09/21/2015	09/03/2018
$M1_2$	77 10.373 125 47.974	783	ADCP SBE	5 – 60 31, 44, 67, 138, 213, 266, 628	09/21/2015	09/03/2018
$M1_3$	77 39.234 125 48.686	1866	ADCP MMP	5 – 55 70 – 1056	09/21/2015 09/22/2015	09/03/2018 06/15/2017
$M1_4$	78 28.084 125 57.679	2700	ADCP ADCP SBE37	5 – 30 155 – 430 38, 107, 188, 240, 604	09/21/2015	09/18/2018
$M1_5$	79 56.194 126 01.228	3443	ADCP MMP	5 – 61 172 – 806	09/21/2015 09/24/2015	08/31/2018 08/29/2018

Accepted for publication in *Journal of Climate*. DOI 10.1175/JCLI-D-19-0976.1.

Mooring M1$_{4-short}$ (September 2 –20, 2018)						
M1$_{4\text{-short}}$	78 30.833 125 58.924	2700	MMP	30 – 194	09/02/2018	09/20/2018
Moorings M3						
M3e	79 56.136 142 14.887	1335	ADCP SBE	5 – 61 41, 45, 57, 64, 130, 270 600	08/31/2013	09/07/2015
M3f	79 56.194 142 15.216	1357	ADCP SBE	5 – 44 30, 50, 133, 217, 268, 614	09/07/2015	09/06/2018

776
777

Accepted for publication in *Journal of Climate*. DOI 10.1175/JCLI-D-19-0976.1.